

The Pennsylvania State University
The Graduate School

NOVEL CARBON-HYDROGEN NANOSTRUCTURES

A Thesis in
Physics
by
Dragan Stojkovic

© 2004 Dragan Stojkovic

Submitted in Partial Fulfillment
of the Requirements
for the Degree of

Doctor of Philosophy

December 2004

The thesis of Dragan Stojkovic was reviewed and approved* by the following:

Vincent H. Crespi
Professor of Physics
Thesis Adviser and Chair of Committee

Kristen A. Fichthorn
Professor of Chemical Engineering

Ari M. Mizel
Assistant Professor of Physics

Peter C. Eklund
Professor of Physics

Jayanth R. Banavar
Professor of Physics
Head of the Department of Physics

*Signatures are on file in the Graduate School.

Abstract

This work concerns design and prediction of properties of carbon and hydrogen materials on the basis of computer simulations. After an overview of the theory behind computational methods used in actual calculations, pure carbon systems are discussed, starting with the traditional carbon materials graphite and diamond and continuing with the novel structures such as nanotubes and nanoporous carbon. For nanoporous carbon we show how non-hexagonal rings introduce electronic aromatic radicals corresponding to additional bands which narrow the band gap. The main part of the thesis contains investigation of interaction between carbon tubular systems and hydrogen. First, physisorption and chemisorption of hydrogen on tubes are discussed. We found that more curved regions of carbon surface have stronger Van der Waals interaction with hydrogen, leading to an increase in physisorption. In chemisorption, if hydrogen is allowed to access the both sides of the carbon surface, the hydrogen cluster becomes favorable after some initial size, due to a collective stabilization of successive adjacent chemisorbed hydrogen atoms mediated by cooperative alternate distortions in the underlying carbon sheet. Afterwards, we show how chemisorption can be used to change mechanical and electronic properties of nanotubes. We present our two original carbon-hydrogen tubular structures, the sp^3 -only tubes and the eye tubes. Small sp^3 tubes are very strong mechanically and insulators electronically, while eye tubes are related to the graphitic ribbons, with unique electronic band structures and a magnetic ground state. The zig-zag eye tubes have band gap sensitive to the applied electric field, while the armchair eye tubes have two very close long flat bands around the Fermi level potentially interesting for terahertz applications. In addition, we propose how those structures could in principle be realized in experiment.

Table of Contents

| | |
|---|------------|
| List of Figures | vi |
| List of Abbreviations | xi |
| Acknowledgments | xii |
| 1 Introduction | 1 |
| 1.1 Basic Formulas | 1 |
| 1.2 Periodic Systems | 3 |
| 2 Methods | 5 |
| 2.1 Tight Binding Method | 5 |
| 2.2 Density Functional Theory | 7 |
| 2.2.1 Local Density Approximation | 11 |
| 2.2.2 Pseudopotentials | 12 |
| Norm-Conserving Pseudopotentials | 14 |
| Ultrasoft Pseudopotentials | 14 |
| 3 Pure-Carbon Systems | 16 |
| 3.1 Traditional Carbon Structures | 19 |
| 3.2 Novel Carbon Structures | 21 |
| 3.2.1 Nanotubes | 21 |
| 3.2.2 Nanoporous Carbon | 24 |
| 4 Carbon-Hydrogen Systems | 29 |
| 4.1 Hydrogen Physisorption on Tubes | 32 |
| 4.2 Hydrogen Chemisorption on Tubes | 37 |
| 4.3 Carbon-Hydrogen sp^3 Tubes | 47 |
| 4.4 Eye Tubes | 54 |
| 5 Conclusion | 63 |

| | |
|----------------------------------|----|
| Appendix: Translational Symmetry | 67 |
| Bibliography | 69 |

List of Figures

| | | |
|-----|---|----|
| 1.1 | Essential steps in the relaxation procedure. | 3 |
| 3.1 | The carbon atom valence energy levels in the ground state (left) and the excited state (right). | 16 |
| 3.2 | Partial charge density on the basis of LDA calculation for the highest occupied orbital of one carbon atom (left) and for two carbon atoms at a separation as in graphene (1.41 Å). | 17 |
| 3.3 | Relaxed configurations for steps in successive dehydrogenization of cyclohexane (left) to benzene (right). Double bonds are indicated with symbol π in cyclohexene structures. | 17 |
| 3.4 | Partial charge density on the basis of LDA calculation for the highest occupied orbital of the CH_3 radical, when carbon is pushed above the plane. Arrows show the response of the electronic density when the bonds bend. | 18 |
| 3.5 | On the left: LDA bands and Brillouin zone structure for graphene. On the right: the partial charge density (equisurface for 0.01 electrons per Å ³) for the Fermi state at K. | 20 |
| 3.6 | Structure, Brillouin zone and LDA bands for cubic (on left) and hexagonal (on right) diamond. The structural images show that the tunnels are similar to the small nanotubes: (3,0) for cubic diamond and (2,2) for hexagonal diamond. | 21 |
| 3.7 | Rolling of a nanotube. An unit cell of (5,2) tube is showed unrolled outlined with dashed lines. Unique atoms in the corresponding ribbon are showed as spheres. In agreement with the nanotube's nomenclature, the circumference of the tube corresponds to the vector $\vec{C} = 5\vec{a}_1 + 2\vec{a}_2$ normal to the axis of the ribbon. Vectors \vec{a}_1 and \vec{a}_2 are basis vectors for the translational symmetry of the hexagonal graphene plane, $\ \vec{a}_1\ = \ \vec{a}_2\ = 1.42 \text{ Å} \cdot \sqrt{3}$ | 22 |

| | | |
|------|--|----|
| 3.8 | The band folding technique forms nanotube bands (shown on right) as combined projection of graphene band slices (lines on the surface), taken across the graphene BZ (hexagon below) along the allowed lines in k-space. | 23 |
| 3.9 | Band structure, density of states and partial charge densities for the (7, 0), (8, 0) and (9, 0) zig-zag and the (6, 6) armchair tube. Due to the calculation method DOS is smeared by 0.1 eV, so it doesn't vanish sharply at the gap nor it has Van Hove singularities. To show the features, DOS is normalized on each graph and absolute DOS values between tubes might be different. The insets are partial charge densities (equisurfaces for 0.003 \AA^{-3}) from LDA calculations for lowest unoccupied (above) and highest occupied (below) states at the Gamma point. All armchair tubes have similar charge density, while there are three types of zig-zag tubes, two semiconducting and one $(3d, 0)$ metallic. | 24 |
| 3.10 | $2 \times 2 \times 2$ unit cells and LDA band plots of a series of d-schwarzite carbon structures. | 25 |
| 3.11 | LDA band plots of C504 d-schwarzite carbon structure with two and five Stone-Wales defects. SW atoms are emphasized as bigger points in the structural image. | 27 |
| 3.12 | LDA band plots of C504 d-schwarzite carbon structure with two chemisorbed hydrogens on the same places where SW defects are in Figure 3.11. | 27 |
| 4.1 | (a) The starting structure, an (8,8) tube with 10% atoms removed and computed nanotube structure with rough walls obtained from simulation of a rapid high-temperature anneal of a damaged tube, as described in the text. Darker carbon atoms exhibit larger deviations from planarity, showing that the distortions propagate outward from pentagonal rings. The darkest region has summed bond angle deficit of 15 degrees on a site between two fused pentagons. A patch with two fused pentagons extracted from such a nanotube is shown in (b), provided courtesy of Jeffrey Grossman, with the relaxed position of a hydrogen molecule above the most distorted carbon atom. The seven-tube bundle shown in cross section in (c) is built from the same tube, but each replica has a random orientation and was allowed to relax to an intertube separation dictated by a standard intertube van der Waals interaction. | 34 |

| | | |
|------|---|----|
| 4.2 | LDA DFT results for the energy ΔE of the hydrogen chemisorption on the (8,8) tube, following the minimal energy path described in the main text. | 40 |
| 4.3 | Tight binding total energy difference ΔE of hydrogen chemisorption following the minimal energy path, as described in the main text. Configurations with negative ΔE are more stable than a corresponding clean carbon structure plus molecular hydrogen. | 41 |
| 4.4 | Sequences of hydrogen atoms chemisorbed by following a minimal energy path for the (8,8) and (12,0) tubes and graphene. Gray disks represent atoms chemisorbed inside the tube or below the sheet. Arrows show the path of successive hydrogen addition. Hydrogen atoms with explicit index numbers are discontinuities in the path. | 41 |
| 4.5 | The final configurations of a sequence of hydrogen atoms chemisorbed by following a minimal energy path. (a) On the smaller-diameter (12,0) tube, the strain on the clean part of the tube induces a new row ((b), side view) to start before the first row circles the belly of the tube. (c) In the (8,8) tube, the cluster again grows as a ring around the circumference. (d) In the graphene sheet, hydrogen atoms arrange in a double zig-zag row. The edge-on view for the graphene sheet emphasizes the sp^3 -like vertical distortions away from the perfectly planar sp^2 starting structure. Schematic top views of the same structures are shown in Figure 4.4. | 42 |
| 4.6 | Difference in the energies ΔE for (8,8) (squares) and (12,0) (triangles) tubes with completed rows of chemisorbed hydrogen. Rows alternate from the outside to the inside of the tube. Four structures (a-d) are detailed in the text. | 44 |
| 4.7 | The proposed precursor (could be CHI_3) and an illustrative growth configuration showing the role of the capping ligand. | 48 |
| 4.8 | Adamantane is an alkane with four fused hexagonal rings. | 49 |
| 4.9 | The relaxed structures of the (2,2) and (3,0) tubes. The (2,2) tube wireframe image shows two unit cells. On sides are space-filling models of the tubular structures. | 50 |
| 4.10 | The electronic band-structures of the (2,2) and (3,0) nanotubes, showing the large bandgap. Residual band folding is visible. The (3,0) tube has weakly dispersive bands due to the rather long axial carbon-carbon bondlength of 1.62 Å. Horizontal axes use the same scale in both plots. | 50 |
| 4.11 | The tight-binding relaxed structure of (a) the (8,8) and (b) the (5,0) sp^3 tube (three unit cells are showed). | 52 |

| | | |
|------|--|----|
| 4.12 | Left: Uniaxial compression of a nanotube transverse to its axis in the presence of hydrogen molecules could facilitate chemisorption onto diametrically opposed rows by forcing these carbon atoms into an sp^3 configuration, as shown on right. The aperture angle θ of the sp^3 junction is used later in the discussion of structural energetics. | 54 |
| 4.13 | (courtesy of Paul Lammert) Chemisorption patterns on (a) zig-zag and (b) armchair nanotubes. Open circles indicate adsorption sites and the absence of an accessible p_z orbital. Heavy bonds symbolize electronic π -hopping in the tight-binding picture; the light bonds are inactive. | 55 |
| 4.14 | PAW GGA band plots with density of states and the electron probability density plots (density isosurfaces for 0.003 \AA^{-3} are shown) for the highest occupied and lowest unoccupied states at Γ for (8,0), (9,0) and (10,0) eye tubes. In each case, the wavefunction has a node on the sp^3 carbon. | 56 |
| 4.15 | Left: PAW GGA spin polarized band structures showing uneven spin population on the Fermi level (blue and black curves represent two spin polarizations) for (6,6) eye tube and its half, a bended (unrelaxed) graphitic ribbon terminated with hydrogens at positions where carbon atoms are in the eye tube. The electron probability density plots for combined spin and spin difference shown on the right (density isosurfaces for 0.003 \AA^{-3} are shown) for the highest occupied and lowest unoccupied states at the gamma point illustrate electronic bifurcation in the eye tube and close connection to the ribbon's edge state. In both cases carbon-carbon bonds in the circumferential direction lengthen gradually from 1.40 \AA at the zig-zag edge to 1.58 \AA at the bearded edge, nearly the same as the change from a double bond to single bond. | 57 |
| 4.16 | (courtesy of Paul Lammert) Upper panel: tight-binding results for the near-Fermi-energy bands of the (6,6) eye tube. The solid line is in zero field, the gray line for $\mathbf{E} = 1 \text{ V/nm } \hat{x}$, and the dashed line for $\mathbf{E} = 1 \text{ V/nm } \hat{y}$. The individual band widths are significantly larger than found in GGA; the band separation is in much better agreement. Lower panel: minimum direct gap between the bands as a function of field. The solid lines are for the (6,6) eyetube and the dashed lines for the (11,0) eyetube. The direction of the field is indicated by x or y . Since the tight-binding calculations are not self consistent, the values of electric field should be interpreted in terms of voltage drop across the eye. | 58 |

| | |
|---|----|
| 4.17 The energy per carbon atom from DFT calculations and the fit of Eq. (4.2) with coefficients given in text for (n, n) and for $(n, 0)$ eye tubes. | 61 |
|---|----|

List of Abbreviations

- BZ Brillouin Zone, page 4.
- DFT Density Functional Theory, page 7.
- DMC Diffusion Monte Carlo, page 35.
- GGA Generalized Gradient Approximation, page 12.
- LCAO Linear Combinations Of Atomic Orbitals, page 5.
- LDA Local Density Approximation, page 11.
- NPC Nanoporous Carbon, page 24.
- PAW Projector Augmented Waves, page 15.
- SW Stone-Wales, page 28.

Acknowledgments

This thesis is a result of many years of work which started in former Yugoslavia and finished in Pennsylvania. During that time I have been accompanied and supported by many exceptional individuals. It is my pleasure to use this opportunity to express my gratitude to all of them.

Between the people directly involved in projects incorporated in this thesis, the most prominent place has my adviser and mentor Prof. Vincent H. Crespi. I am happy that I had opportunity to be in a group of such an extraordinary scientist. Many thanks go to my collaborators, particularly to Peihong Zhang and Paul Lammert for sharing their knowledge regarding molecular simulations, to Jeffrey Grossman for his help regarding Diffusion Monte Carlo and to Prof. Peter Eklund and members of his group for keeping our calculations close to a firm ground of experiment.

I also wish to thank to my colleagues, alumni and present members of Crespi's, Cole's and Mizel's groups for a friendly working environment and a great time we spent together in State College. Especially I am obligated to Prof. Jorge Sofo, who is in many ways my second mentor, and to Paul Lammert who, between other things, persisted in a role of an unofficial reader of the thesis draft, giving many profound suggestions regarding physics and mathematics in addition to the English style and grammar.

The limited space prevents me from mentioning here many other names and various ways how people contributed to this development, before all others my parents and sister with all their love and support in difficult times and my former wife who brought me to America.

Chapter 1

Introduction

This chapter presents an (incomplete) overview of the theoretical basis behind the calculational methods presented latter. Its main purpose is to introduce ideas and notation used latter in this work.

1.1 Basic Formulas

The atom seen as a nucleus surrounded by electrons is already quite a complicated object for practical calculations. As always in science, it is important to make a model which captures only important effects and abstracts the rest of the system. The first layer of abstraction in materials modeling is to divide an atom into valence electrons, which contribute to the chemical bonding and the core electrons, which are too deep in the atom for any significant role in the materials chemistry (except for the requirement that the valence states must be orthogonal to the core states). The nucleus and core electrons are then described as ionic core, a rigid object influencing the valence electrons through its net charge. In addition to simplifying calculation, the core concept also increases the accuracy, since tiny energetic effects are more visible on the energy scale of 10^1 Rydbergs (as for valence electrons), than on 10^3 Rydbergs (as a typical energy of all electrons in an atom). This division, however, is more problematic for heavier atoms, where the distinction between core and valence electrons is not as sharp and depends on the environment.

In this (non-relativistic) picture the Hamiltonian of matter is given by:

$$H = T_I + T_e + V_{II} + V_{Ie} + U, \quad (1.1)$$

where T_I is the kinetic energy of ionic cores, T_e is the kinetic energy of the valence electrons and V_{II} , V_{Ie} and U are the ion-ion, ion-electron and electron-electron Coulomb interaction terms.

The Hamiltonian (1.1) incorporates two subsystems with very different time scales. Since ionic cores are much (thousands of times) heavier than electrons, the electronic subsystem evolves so much faster than ions that for the electronic dynamics ions are practically fixed in space. While ions move, the electronic subsystem almost instantly conforms to its ground (equilibrium) state along the ionic path. The resulting equilibrium electronic configuration for the current position of ions then produces an effective potential affecting ionic dynamics.

In the formalism, this observation is formulated as the Born-Oppenheimer (adiabatic) approximation, i.e. the assumption that the eigenstates of (1.1) can be found by focusing on the electronic eigenproblem with ionic positions as parameters. First, the ground state for the electronic subsystem $E_{el}(\mathbf{R}_I)$ should be found as the lowest eigenstate of the Hamiltonian $H_e(\mathbf{R}_I) = T_e + U + V_{Ie}(\mathbf{R}_I)$, which depends on the ionic positions as parameters. Once $E_{el}(\mathbf{R}_I)$ is known, the ground state of the system with ions at rest can be found by minimizing

$$E(\mathbf{R}_I) = V_{II}(\mathbf{R}_I) + E_{el}(\mathbf{R}_I) \quad (1.2)$$

with respect to the set of ionic positions \mathbf{R}_I .

The main complication in this prescription (called also the relaxation procedure) comes from the fact that it contains two interdependent self-consistent problems (Figure 1.1): the electronic subsystem is described by an integro-differential (Schrödinger) equation, which itself must be solved self-consistently for each step in the outer ionic relaxation loop.

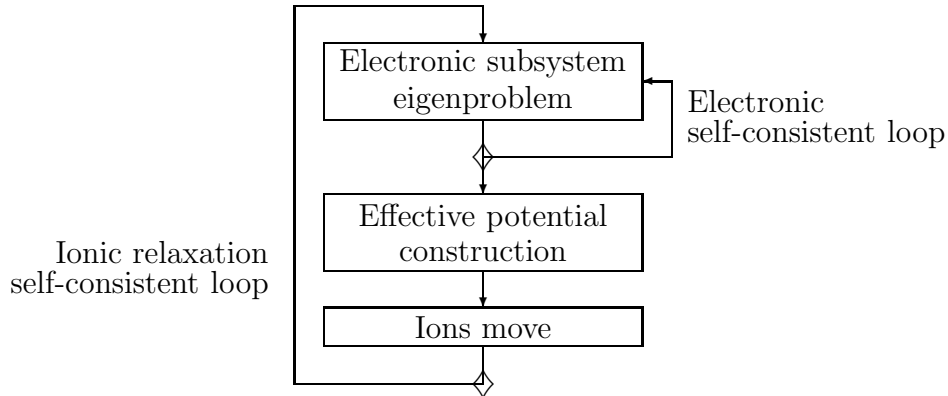


Figure 1.1. Essential steps in the relaxation procedure.

1.2 Periodic Systems

In analysis of physical systems it is always helpful to make an effort to understand and properly implement the symmetry. First of all, electrons have intrinsic symmetry of indistinguishable fermionic particles, which is reflected in the formalism as the requirement that the total wavefunction must be antisymmetric with respect to permutations of electronic coordinates. The full system's wavefunction is, however, never used in actual calculations, since set of electrons is, as any other many-body interacting system, too complicated to be dealt with directly. Theoretical physics in a large measure is an art of the proper reduction of complicated unsolvable systems to one or two particle (the only two analytically solvable) models. In order to produce a good model, this reduction process should preserve important properties of the starting system — before others, its symmetry. The next chapter discusses one particular highly successful way to reduce the interacting electron system to a single particle problem. Let us at this moment assume that it has been already done and focus on consequences of additional symmetries the single particle (model) system might have.

In this work various translationally periodic systems will be discussed. They are completely determined by the unit cell and the set of primitive translations. Quantitative description of this intuitive understanding is based on group theory. Among other results, theory (more details are given in the Appendix 5) shows that

the best basis to use in describing a periodic (one particle) system is a collection of plane waves $\exp(-i\vec{k} \cdot \vec{r})$, where the wave vector \vec{k} belongs to the (first) Brillouin zone (BZ) of the lattice. As a consequence of periodic symmetry, wave vectors do not change in the system's evolution (they are good quantum numbers) and they label eigenstates of the periodic system. However, the wave numbers are not enough to count all eigenstates. There is in fact an infinite dimensional subspace of states for each wave vector and an additional quantum number n should be introduced to index the eigenbasis in that space. All energies (eigenvalues) for the same n and all possible \vec{k} form an energy band as an energy surface (function) above the BZ. Each eigenstate $\varphi_{\vec{k}n}(\vec{r})$ of a periodic system must have periodic amplitude and changes only phase from one to the other unit cell for amount $\vec{k} \cdot (\vec{a}_1 - \vec{a}_2)$, where \vec{a}_j is position of the cell j (Bloch theorem).

A periodic system can be more than just translationally symmetric. The full symmetry of the crystal can always be shown as some kind of product between the translational group and some point group¹. This additional symmetry, if used properly, helps to further reduce the necessary calculations.

Periodic calculations involve integrations of the functions over the crystal. If the functions involved are periodic, the integration can be carried out substantially more easily in \vec{k} -space ("inverse space"), where it translates to a sum of the Fourier coefficients.

A more complicated problem is how to deal with integrations in the inverse space. For example, the total electronic energy of the crystal is given by $E = \sum_n \int f(\vec{k}) E_n(\vec{k}) d^3\vec{k}$, where $f(\vec{k})$ is the occupation factor and $E_n(\vec{k})$ is the band energy. Here summation is over the bands and integration is over the Brillouin zone. Since calculation of values like $E_n(\vec{k})$ is very expensive, an approximate method has been developed [2], which replaces integration over the Brillouin zone with summation over a special set of \vec{k} points, chosen such that the result is as accurate as possible. Monkhorst and Pack [2] showed that the best set of points is an equally spaced lattice $\vec{k}_{prs} = u_1\vec{b}_1 + u_2\vec{b}_2 + u_3\vec{b}_3$, where coefficients are $u_j \in \{(2r - q_j - 1)/2q_j | r = 1, 2, \dots, q_j\}$ and q_j is the number of special points along direction \vec{b}_j .

¹All elements of the point group leave at least one point intact when they act in the space.

Chapter 2

Methods

In the past several decades, as available computer power increased, a broad range of methods for numerical studies of materials has been developed, each of them good for specific uses. In this work we are concerned with the total energy and electronic properties of carbon-hydrogen systems. Both carbon and hydrogen are small, relatively simple atoms and can be (under some conditions) reasonably modeled with almost any quantum based computational method. Depending on the size of the system, investigated property and targeted accuracy, in actual calculations we used tight binding and density functional based methods.

2.1 Tight Binding Method

The tight binding method solves the double self-consistent problem difficulty mentioned in section 1.1 in a simplest possible way, completely avoiding self-consistent electronic calculation. Instead, the electronic wavefunctions are approximated as linear combinations of atomic orbitals (LCAO method):

$$\psi_i(\vec{r}) = \sum_{\nu} C_{\nu i} \varphi_{\nu}(\vec{r} - \vec{R}_{\nu}), \quad (2.1)$$

where index ν goes through all included atomic orbitals on all atomic sites in the system, $C_{\nu i}$ are to-be-determined linear combination coefficients and \vec{R}_{ν} is atomic site position for orbital ν . In order to have better numerical convergence, contracted atomic orbitals φ_{ν} are usually used [4], which have the correct shape,

but decay faster than the exact wavefunctions.

The Schrödinger equation then takes a matrix form

$$(\mathbf{H} - \epsilon_i \mathbf{S}) \mathbf{C}_i = 0, \quad (2.2)$$

where \mathbf{C}_i is a vector of coefficients from (2.1) and \mathbf{S} is the overlap matrix with elements $S_{\mu\nu} = \int dr \varphi_\mu^*(\vec{r} - \vec{R}_\mu) \varphi_\nu(\vec{r} - \vec{R}_\nu)$. Detailed analysis [3] shows that for transferability of tight binding parameters (their ability to describe atoms in different environments) it is essential to have non-orthogonal ($\mathbf{S} \neq 1$) atomic orbital set. Despite the severe approximation (2.1), the hamiltonian matrix elements

$$H_{\mu\nu} = \int dr \varphi_\mu^*(\vec{r} - \vec{R}_\mu) H \varphi_\nu(\vec{r} - \vec{R}_\nu) \quad (2.3)$$

are still very hard to calculate, since they include up to three-center integrals (which happens when the orbitals and the electronic-ion potential term in (1.1) are all centered on different atoms).

Slater and Koster [5] developed a way to fit the hamiltonian matrix elements (2.3) with the two-center-only form. If more accurate density functional theory is used for the fit, the explicit expression is [4]:

$$H_{\mu\nu} = \begin{cases} \varepsilon_\mu \delta_{\mu\nu}, & \text{if } \mu = \nu \\ \int dr \varphi_\mu^*(\vec{r} - \vec{R}_\mu) (T + V_{\text{KS}}^{(\mu)} + V_{\text{KS}}^{(\nu)}) \varphi_\nu(\vec{r} - \vec{R}_\nu), & \text{if } \mu \neq \nu \end{cases} \quad (2.4)$$

where ε_μ is the on-site energy and $V_{\text{KS}}^{(\mu)}$ is the Kohn-Sham potential (discussed in detail in next section) for atomic orbital μ (index μ uniquely defines the host atom for that orbital).

Once the generalized eigenproblem (2.2) is solved, resulting in a set of energies ϵ_i , the energy of the system can be found as

$$E_{\text{total}} = \sum_i \epsilon_i f(\epsilon_i) + F, \quad (2.5)$$

where $f(\epsilon_i)$ is the electron population of the level ϵ_i and F is a short-ranged ionic repulsive correction term, which also can be fit using density functional calculation [4].

The prescription presented here is called the non-orthogonal density functional-based tight binding method. Since the LCAO description of the electronic subsystem is very rigid, the tight binding method has a lower accuracy than most of the other quantum-based methods (for example, the total energy error is usually within 10-15%), but is also the least demanding and can be applied on massive systems containing thousands of atoms. In addition to that, the abstraction of the electronic subsystem, as it is done in the tight-binding, can actually lead to a better understanding of the relevant physics, if it is not related to the fine details of the electronic structure. In the case of simple small atoms (the first row in the periodic table), this approach with carefully chosen atomic orbitals gives also reasonably accurate results. Carbon, hydrogen, oxygen and nitrogen are all first row elements, so many of the organic compounds can be satisfactorily well described in the frame of the tight binding method.

2.2 Density Functional Theory

In order to make more reliable description of materials, one must develop a precise model of the electronic subsystem. In the usual quantum mechanical picture, basic objects are wavefunctions and operators in the functional space. Neither is suitable for detailed description of many-body systems. For example, a crude estimate for a system of $N = 100$ interacting electrons gives a hopeless number of 10^{150} [6] parameters needed to develop a modestly precise (with relative error of the order of 10^{-1}) variational wavefunction. This “exponential wall” shows that the problem is not in our current technical (computing) capabilities, but within the approach itself¹.

Regarding operators in the functional space, they all contain much more information than we need to describe our specific system. For example, the hamiltonian has an infinite number of eigenstates, but we usually need to describe a system only in its ground state and maybe its first several excited states.

The density functional theory (DFT) is an alternative description of a system

¹In his Nobel lecture W. Kohn comments on this problem using words of his teacher, J. H. Van Vleck [6]: “In general the many-electron wave function $\Psi(r_1, \dots, r_N)$ for a system of N electrons is not a legitimate scientific concept, when $N \geq N_o$, where $N_o \approx 10^3$.”

of bound interacting electrons, where instead of wavefunctions and operators, the basic objects are the ground state probability density and appropriate functionals. This approach is possible due to two fundamental theorems proven by P. Hohenberg and W. Kohn [7]:

- For any bound system of interacting electrons in some external potential $V_{ext}(\vec{r})$, the ground state density $n(\vec{r})$ determines this potential uniquely (up to an additive constant).
- For any particular external potential $V_{ext}(\vec{r})$, the exact ground state density and the exact ground state energy are the global minimum coordinates of the energy seen as functional of density (such functional exists due to the first theorem).

As a consequence of the first theorem, because any system of interacting electrons is uniquely defined by the number of particles and the external potential, the ground state density completely determines everything about the system, including hamiltonian and all excited states. That assures that the variational energy functional is always well defined in the second theorem.

The proof of these two theorems by reduction to a contradiction is very simple, but not constructive. In order to make a practical method out of the density functional theory, Kohn and Sham [8] started from the basic ground state energy variational principle. Their construction shall be presented here in a more elegant and general way due to Levy [9].

As the variational principle says, the ground state energy and the ground state wavefunction are coordinates of the global minimum of the functional $\langle \Psi | H | \Psi \rangle$ over all normalized wavefunctions Ψ . Since every trial wavefunction $\tilde{\Psi}$ corresponds to only one density \tilde{n} , the variational search can be carried on in two steps: first by finding infimum²

$$E[\tilde{n}] = \inf_{\alpha} \langle \Psi_{\tilde{n}}^{\alpha} | H | \Psi_{\tilde{n}}^{\alpha} \rangle, \quad (2.6)$$

over all wavefunctions $\Psi_{\tilde{n}}^{\alpha}$, which produce the same density \tilde{n} and then finding minimum of those infimums, i.e. minimizing the functional $E[\tilde{n}]$, which is already

²There is a subtle difference between infimum and minimum. Infimum exists for any set, what is not true for minimum. However, if minimum exists (as we know in this case), then it is also always the infimum of a set. Since the Levy's construction introduces subsets of auxiliary wavefunctions, in general it is safer to use infimum in definition of $E[n]$.

defined as result of (constrained) minimization. The external potential doesn't depend on \tilde{n} , so that the ground state is

$$E_o = \min_{\tilde{n}} E[\tilde{n}] = \min_{\tilde{n}} \left\{ \int V_{ext}(\vec{r}) \tilde{n}(\vec{r}) d^3\vec{r} + F[\tilde{n}] \right\}, \quad (2.7)$$

where $F[\tilde{n}] = \inf_{\alpha} \langle \Psi_{\tilde{n}}^{\alpha} | (T_e + U) | \Psi_{\tilde{n}}^{\alpha} \rangle$ (T_e and U are defined in 1.1) is a *universal* functional, an intrinsic characteristic of interacting electrons, which doesn't depend on the environment.

The universal functional $F[\tilde{n}]$ contains kinetic energy and internal potential, i.e. all the complexity of the wavefunction and operators in the usual quantum picture are encapsulated in $F[\tilde{n}]$. This complexity comes not only from potential operators, but also from the wavefunction of interacting electrons, so that the kinetic term $T[\tilde{n}] = F_{U=0}[\tilde{n}] = \langle \Psi_{\tilde{n}}^{\alpha} | T | \Psi_{\tilde{n}}^{\alpha} \rangle$ is also in general a very complicated object. It becomes simple sum of kinetic energies of particles only if $\Psi_{\tilde{n}}^{\alpha}$ is a Slater determinant of one-particle states, as for non-interacting particles. In that case, the true non-interacting ground state is always a Slater determinant and the variational search can be constrained from the beginning to Slater determinants only.

In the next, crucial, step let's take a pragmatic approach and extract from the universal functional everything we know how to deal with:

$$F[\tilde{n}] = T_s[\tilde{n}] + \frac{1}{2} \int \int \frac{\tilde{n}(\vec{r}) \tilde{n}(\vec{r}')}{\|\vec{r} - \vec{r}'\|} d^3\vec{r} d^3\vec{r}' + E_{xc}[\tilde{n}], \quad (2.8)$$

where:

- $T_s[\tilde{n}]$ is functional which maps \tilde{n} into kinetic energy of the system of *non-interacting* particles with the density \tilde{n} . The first HK theorem guarantees³ that this functional is well defined. Also, it is worth noting that the kinetic energy functionals $T[\tilde{n}] = F_{U=0}[\tilde{n}]$ and $T_s[\tilde{n}]$ are different objects: they have the same kinetic operator in their definition, but they are sandwiched with different wavefunctions. Since we are dealing with functionals, it is perfectly valid to extract from $F[\tilde{n}]$ part which represents functional for some other, in

³Under assumption of so-called V-representability of the given density, which seems to be valid for all physically meaningful systems.

this case non-interacting system, as far as the functional argument (density) is the same.

- The term with integral is the Hartree part of the electronic interaction, which is the only part of the universal functional $F[\tilde{n}]$ with a known explicit expression in terms of density.
- $E_{xc}[\tilde{n}]$ is called the exchange correlation functional and it contains everything that is left in $F[\tilde{n}]$ besides the above two functionals. It contains remains of both kinetic and potential parts. The exact form of the exchange correlation functional is unknown and it must be approximated on the basis of the physics of the system in question. The key to the success of DFT is the fact that $E_{xc}[\tilde{n}]$ is (for a wide range of systems) much smaller than the other two parts of the universal functional.

Using (2.8) the expression for energy (2.7) can be rewritten in a non-interacting system form:

$$E_o = \min_{\tilde{n}} \left\{ T_s[\tilde{n}] + \int V_{eff}(\vec{r}) \tilde{n}(\vec{r}) d^3\vec{r} \right\}, \quad (2.9)$$

where V_{eff} is kernel of the functional $\int V_{ext}(\vec{r}) \tilde{n}(\vec{r}) d^3\vec{r} + \frac{1}{2} \int \int \frac{\tilde{n}(\vec{r}) \tilde{n}(\vec{r}')}{\|\vec{r} - \vec{r}'\|} d^3\vec{r} d^3\vec{r}' + E_{xc}[\tilde{n}]$. However, we know how to find the ground state density of the non-interacting system: it is enough to find eigenstates φ_j of the *one-particle* hamiltonian

$$H_1 = -\frac{1}{2} \nabla^2 + V_{eff} \quad (2.10)$$

and the ground state density is given by $n_o = \sum_j |\varphi_j|^2$. According to the construction, this is also the ground state density of the fully interacting system.

In this way the above Kohn-Sham construction leads to the ground state density of an interacting electron system solving an auxiliary one-particle hamiltonian eigenproblem with an effective external potential.

By applying the functional derivative, a more explicit formula for V_{eff} can be established as $V_{eff}(\vec{r}) = V_{ext}(\vec{r}) + \int \frac{n_o(\vec{r}')}{\|\vec{r} - \vec{r}'\|} d^3\vec{r}' + V_{xc}(\vec{r})$, where $V_{xc} = \frac{\delta}{\delta \tilde{n}} E_{xc}[\tilde{n}]|_{\tilde{n}=n_o}$. Since V_{eff} is expressed in terms of the ground state density n_o , the one-particle hamiltonian eigenproblem needs to be solved self-consistently.

Strictly speaking, the eigenstates of the auxiliary hamiltonian (also called

Kohn-Sham orbitals) separately have no physical meaning. However, since they are density-optimized one particle states, they usually well resemble chemically acceptable molecular orbital shapes for different levels in molecules and bands in crystals and are widely used for charge density analyses.

Similarly, the eigenvalues of the auxiliary hamiltonian (Kohn-Sham orbital energies) have no physical meaning except that the energy of the highest occupied Kohn-Sham orbital is equal to the ionization energy of the system. Despite that, it is empirically proven that the auxiliary non-interacting spectrum resembles to some extent the energy levels of interacting electrons and it is particularly common to consider DFT band plots in discussion of periodic structure electronic properties.

2.2.1 Local Density Approximation

The only missing piece in the Kohn-Sham construction is the exchange-correlation functional $E_{xc}[n]$. The general form of this functional is not known, but its extreme case, when the function $n(\vec{r})$ is uniform, can be calculated. When n is a constant, the exchange-correlation functional becomes a function $E_{xc}(n)$ describing the uniform electron gas exchange-correlation energy. Even in this simplest case, the energy function $E_{xc}(n)$ can be found only numerically, on the basis of a Monte Carlo simulation⁴.

In the general case, density n is a function of the position \vec{r} and the functional $E_{xc}[n]$ has an unknown form, but the uniform electron gas result can still be used as part of the *local* density approximation (LDA) of the exchange-correlation functional as $E_{xc}^{LDA}[n] = \int e_{xc}(n(\vec{r})) n(\vec{r}) d^3\vec{r}$, where $e_{xc}(n(\vec{r}))$ is the uniform electron gas exchange-correlation energy per particle.

More careful analysis [11] shows that for the actual calculations some global properties (angular average and sum rules) of the exchange-correlation functional are more important than its detailed shape. Since the uniform electron gas is a real (although quite idealized) system of interacting electrons, the LDA based on it satisfies all these requirements. That explains why although the uniform gas is a very simplified model of the general electronic system, in practice LDA gives for

⁴More precisely, the exchange part has an analytical form, but that is not true for the correlation part, first numerically calculated by Ceperley [10] using Monte Carlo method. As an alternative, the correlation part can be calculated using Feynman diagrams summation.

a wide range of systems quite accurate results.

The LDA gives very accurate results for the geometry: it predicts bond lengths and bond angles usually within around 1% relative error to the experiment. The LDA energy error is on the order of 5-10% and this approximation systematically overbinds the atoms. For periodic systems, LDA gives bands usually with correct shapes, but distances between them are systematically underestimated. Some materials are even predicted to be metals, while they are semiconductors (one example is germanium).

In more complicated cases, like magnetic or heavy fermion systems, LDA (and local spin density approximation (LSDA), the version with unpaired spins) becomes qualitatively inaccurate. For example, LSDA predicts that the iron has a non-magnetic fcc lattice ground state, in contrast to the experimental magnetic bcc Fe ground state.

Having in mind all these shortcomings, a number of other DFT methods have been developed, most notably the generalized gradient approximation (GGA) [11]. However, LDA remains the method of choice for many materials, especially if they contain only simple atoms, such as carbon and hydrogen, as in our case.

2.2.2 Pseudopotentials

As discussed in the Introduction, one simplification in the description of materials comes from the division of atoms into core and valence electrons. In addition to that, DFT gives a way to reduce system to one particle hamiltonian (2.10) eigenproblem. Despite all these simplifications, the valence wavefunctions are still too complicated in the core region for practical calculations. Fortunately, there is room for further approximation, allowed by the fact that for chemical properties only the part of electronic wavefunction outside of the core electron region is important. Hence, without losing chemical accuracy, it is possible to replace the true valence wavefunction with a better behaving pseudowavefunction, which is the same as the true wavefunction outside the core and smoother in the core region. The smoothness of the pseudowavefunction is especially important in periodic systems, since a smoother function requires fewer plane waves in the basis.

One way to construct the pseudowavefunction $|\tilde{\psi}_v\rangle$ is to subtract a linear

combination of core states $\sum_c \alpha_c^v |\phi_c\rangle$ from the true valence wavefunction $|\psi_v\rangle$. Then the difference $|\psi_v\rangle - |\tilde{\psi}_v\rangle = \sum_c \alpha_c^v |\phi_c\rangle$ vanishes outside the core, since the core wavefunctions are essentially non zero only inside the core radius.

Using the fact that all core and valence states are mutually orthogonal (as a consequence of the Hamiltonian hermiticity):

$$0 = \langle \phi_c | \psi_v \rangle = \langle \phi_c | \tilde{\psi}_v \rangle + \alpha_c^v \Rightarrow \alpha_c^v = -\langle \phi_c | \tilde{\psi}_v \rangle \quad (2.11)$$

and the fact that the true valence state $|\psi_v\rangle = |\tilde{\psi}_v\rangle + \sum_c \alpha_c^v |\phi_c\rangle$ is an eigenstate of the Kohn-Sham Hamiltonian (2.10):

$$H_1 |\psi_v\rangle = E_v |\psi_v\rangle \Rightarrow H_1 |\tilde{\psi}_v\rangle + \sum_c \alpha_c^v (E_c - E_v) |\phi_c\rangle = E_v |\tilde{\psi}_v\rangle, \quad (2.12)$$

we have:

$$\left(H_1 + \sum_c (E_v - E_c) |\phi_c\rangle \langle \phi_c| \right) |\tilde{\psi}_v\rangle = E_v |\tilde{\psi}_v\rangle. \quad (2.13)$$

That means, although $|\tilde{\psi}_v\rangle$ is not an eigenstate for the original Hamiltonian, it is an eigenstate of a modified Hamiltonian with the pseudopotential $V_{ps} = V + \sum_c (E_v - E_c) |\phi_c\rangle \langle \phi_c|$ instead of the original potential V . Since the valence energy E_v (also called the local energy for the pseudopotential) is always bigger than the core energy E_c , the core sum is always repulsive and partially cancels the attractive potential V (this fact is called cancellation theorem), such that V_{ps} has much smaller magnitude than the original V , producing much smoother eigenfunction $|\tilde{\psi}_v\rangle$.

As an interesting consequence of the effectively weak pseudopotential in crystals, the valence bands are almost free-electron-like, resolving the paradox [3] that for many crystals the valence bands are almost parabolic, although the valence wavefunctions cannot be similar to the plane waves.

The above pseudopotential reformulation of the Schrödinger equation for valence states offers a freedom to choose in actual calculations the numerically best-behaving form of the wavefunction among linear combinations of the valence and all core states.

Norm-Conserving Pseudopotentials

Beside smoothness, a good pseudowavefunction should also be transferable, i.e. it should be an accurate approximation of the true valence wavefunction regardless of the atomic environment. It can be shown [3] that this property is best satisfied if the net charges inside the core region of the true and pseudowavefunction are the same:

$$\int_{\|\vec{r}\| < R_c} |\tilde{\psi}_v|^2 d^3\vec{r} = Q = \int_{\|\vec{r}\| < R_c} |\psi_v|^2 d^3\vec{r}. \quad (2.14)$$

The pseudopotential associated with such a pseudowavefunction is called the norm-conserving pseudopotential.

The norm-conservation property also implies orthonormality of the valence states, which simplifies actual calculations. This method has been developed further by numerically inverting the Schrödinger equation [12] in order to find the pseudopotential starting from a chosen pseudowavefunction and by approximating the pseudopotential in the form of a sum of suitable factors (“separable form”) [13], so that it requires fewer integrations in the actual calculation.

The generation of the pseudopotentials, however, remains a bit of art on its own. The process starts by solving the all-electron Schrödinger equation for the atom alone. Then it should be decided which states are in the core and what is the right cutoff radius for the valence wavefunctions. The cutoff radius should be between last node and maximum of the the true wavefunction, not too big (it harms transferability) and not too small (the pseudowavefunction is then not so smooth). Often there is no one best choice. Rather, it depends on the environment in which atom model will be used.

Ultrasoft Pseudopotentials

In order to make smoother pseudowavefunctions, one should release the norm conservation constraint. In order to keep good transferability properties of the resulting charge conservation violating pseudopotential, Vanderbilt [14] and Blöchl [15] introduced the charge correction term in the Hamiltonian, defined by the matrix

$$\Delta Q_{vv'} = \int_{\|\vec{r}\| < R_c} (\psi_v^* \psi_{v'} - \tilde{\psi}_v^* \tilde{\psi}_{v'}) d^3\vec{r}, \quad (2.15)$$

where ψ_v is either the true valence wavefunction or a norm-conserving pseudowavefunction and $\tilde{\psi}_v$ is the ultrasoft pseudowavefunction. This additional Hamiltonian term describes rapidly varying part of the electron density around each ion core, leaving the ultrasoft wavefunction free of the norm-conservation requirement. At the same time, this formalism allows more than one local energy per quantum state, which additionally increases transferability.

As a drawback, the pseudopotential generation is more complicated and the resulting ultrasoft pseudowavefunctions are not orthogonal, so that a generalized eigenproblem similar to (2.2) of the Hamiltonian (modified with charge correction term) must be solved.

The ultrasoft pseudopotentials require no more than 50-100 plane waves per atom, even for the difficult cases, allowing ab-initio treatment of periodic systems with several hundreds of atoms in the unit cell.

The ultrasoft formalism was also important as a pointer in the right direction for further development of the electronic calculation methods. It is a direct predecessor of the projector augmented waves (PAW) method [16], which keeps the all-electron wavefunction in the calculations. In the case of carbon and hydrogen, the ultrasoft pseudopotentials give sufficiently accurate results, while the formalism can be applied to much bigger systems than the norm-conserving pseudopotentials. At the same time calculations are faster and simpler than more precise methods such as PAW.

Chapter 3

Pure-Carbon Systems

Carbon is an atom with six electrons, four of them contributing to the chemical bonding. The atom's ground state has a filled 2s orbital and two occupied 2p orbitals. However, the energy difference between the ground state and the excited state, in which all four electrons are unpaired and have the same energy, is small, as shown in Figure 3.1. This is because the excited atom also has a quite stable structure with all subshells half-filled. During chemical reactions the energy released in the making of chemical bonds is already large enough to raise carbon to this excited state. As a result, a carbon atom can make four bonds with atoms around it. In that case bonds tend to be in a tetrahedron-like star orientation, which is called sp^3 hybridized state.

The carbon atomic radius is small enough that when two carbon atoms make a bond, they are close enough to have a significant overlap not only between orbitals pointing toward each other (they make σ bond), but also between the other p orbitals. This overlap is so big that electrons in p orbitals can make strong

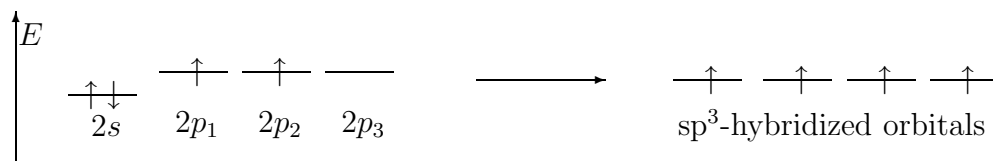


Figure 3.1. The carbon atom valence energy levels in the ground state (left) and the excited state (right).

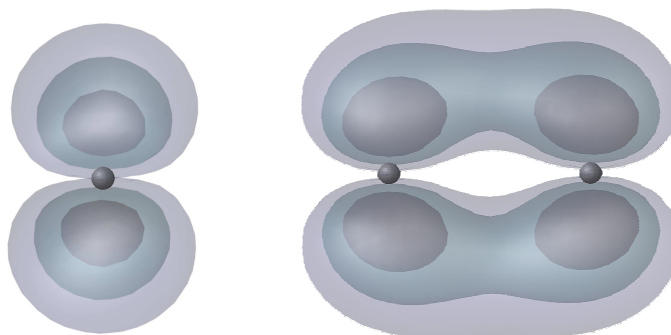


Figure 3.2. Partial charge density on the basis of LDA calculation for the highest occupied orbital of one carbon atom (left) and for two carbon atoms at a separation as in graphene (1.41 Å).

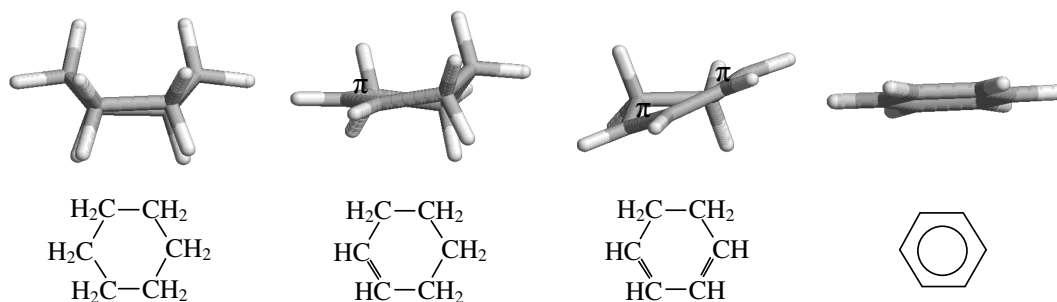


Figure 3.3. Relaxed configurations for steps in successive dehydrogenization of cyclohexane (left) to benzene (right). Double bonds are indicated with symbol π in cyclohexene structures.

additional π bond (Figure 3.2): while the C-C σ bond has¹ 3.5 eV binding energy, the C-C π bond has around 2.6 eV. Hence, carbon can also make stable bondings with only two or three neighbors, pairing extra electrons in π bonds with other atoms.

The case with three bonds is called the sp^2 hybridized state. Three sp^2 bonds are in one plane, with equal angles between them. The fourth electron remains equally distributed above and below that plane, paired in a π bond with such an electron from a neighboring atom. The π bonds across the structure tend to be in resonance with each other, reinforcing the planar network. This reinforcement significantly changes properties of the carbon structure. For example, if in cyclohexane (a ring with 6 single-bonded carbon atoms, Figure 3.3) one or two single

¹1 eV/molecule = 23.045 kcal/mol or 1 kcal/mol = 43.4 meV/molecule.

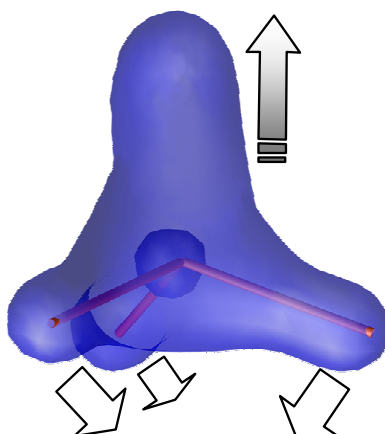


Figure 3.4. Partial charge density on the basis of LDA calculation for the highest occupied orbital of the CH_3 radical, when carbon is pushed above the plane. Arrows show the response of the electronic density when the bonds bend.

bonds are replaced with the double bonds (in a successive dehydrogenization), the double bonds behave much like in hexene or any other alkene. However, when the third double bond is introduced in the ring, a radical change in the electron distribution occurs. The carbon atoms now lie in a plane, as a contrast to the cyclohexane and cyclohexene structures. All carbon-carbon bonds and all carbon-hydrogen bonds become identical in length and reactivity. The resulting structure is much more stable: halogens and hydrogen cannot be added to it as easily as before, nor it is easily oxidized. This qualitatively new ring structure is called benzene and is often represented by a circle rather than alternating single and double bonded hexagon sides. Benzene is the simplest of the *aromatic* hydrocarbons, which have the π bonding electrons rearranged in benzene-like rings instead of alternating single and double bonds.

Pure sp^2 or sp^3 carbon states form when the strains imposed by the surrounding carbon super-structure are minimal. However, in materials with additional nanometer-scale structural constraints, (such as a requirement to maintain a tubular circumferential integrity in nanotubes), the resulting constraint forces can impose bonding geometries that deviate significantly from the ideal sp^2 and sp^3 bond angles. In that situation the π electrons redistribute, concentrating more outside the bent regions (from the positive curvature side, Figure 3.4).

A double bond is always stronger than a single bond, which is reflected in

the equilibrium distances between atoms. For carbon, the single bond distance is 1.54 \AA (for example, in diamond), while the carbon double bond in C_2H_6 has a length of just 1.33 \AA . Bending weakens bonds and increases distance between atoms.

Although under special conditions, other atoms (for example, silicon) can make double bonds, those additional bonds are almost always less stable than in carbon. One exception is nitrogen, which has very strong triple bond in the N_2 molecule. Carbon's ability to make multiple bonds leads to the uniquely rich carbon chemistry and makes this element the central brick in the building of life.

3.1 Traditional Carbon Structures

Until the 1980's, carbon was known to exist in only two allotropes: graphite and diamond. Graphite is the most stable carbon structure. It exists in two forms, as planar and rhombohedral graphite [59]. Only the planar form is considered here.

The sp^2 hybridized carbon connects in graphite hexagonal planes using three of its valence electrons to make in-plane σ bonds. The remaining p electrons (one per atom) form highly delocalized π pairs which resonate between atoms. Therefore, the in-plane bonds are stronger than the single carbon bond (in-plane distance between atoms is 1.42 \AA instead of 1.54 \AA in diamond). Neighboring planes are far apart (3.35 \AA) and only weakly bound due to the overlap of the π electrons and the Van der Waals interaction.

The density functional theory within local density approximation (LDA DFT) cannot describe properly the weak interlayer interaction in graphite (it predicts an unphysically large distance between layers), but it can be applied to one isolated hexagonal sheet of graphite (*graphene*). The graphene structure is important since it can be considered as a basis for nanotubes and similar carbon structures.

The graphene DFT band structure is shown in Figure 3.5. Graphene is a zero gap semiconductor, with bands touching at the corners of the hexagonal Brillouin zone (the K points). The density of states at the Fermi level is zero, so graphene is a weak metal (semimetal). Due to a weak interaction between layers, graphite has practically the same in-plane band structure as graphene and a semigap along the c axes, normal to the hexagonal planes.

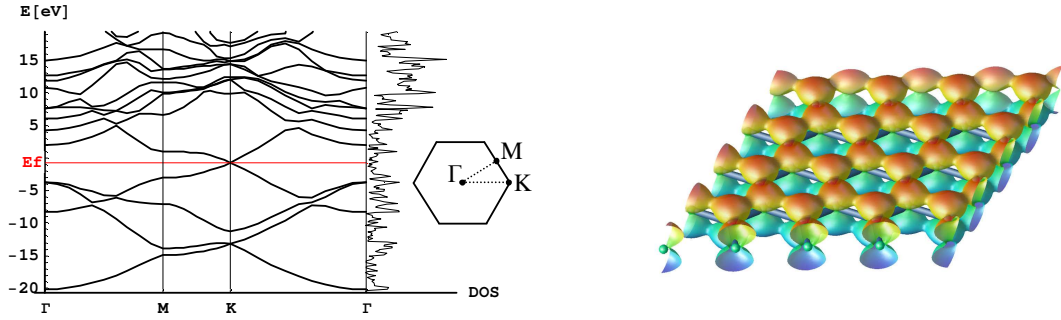


Figure 3.5. On the left: LDA bands and Brillouin zone structure for graphene. On the right: the partial charge density (equisurface for 0.01 electrons per \AA^3) for the Fermi state at K.

Diamond structurally has a higher energy per atom than graphite. However, the energy barrier for its graphitization is very high. Thus, diamond is kinetically a very stable structure².

There are two allotropic modifications of diamond, Figure 3.6. A common form is cubic diamond, which has an fcc lattice with two atoms in the unit cell. The other form is hexagonal diamond, which has been found only in some meteorite impact sites. Both varieties have been also synthesized in the laboratory.

As a consequence of single carbon covalent bonding in a tetrahedron structure, diamond is very hard and a very good insulator. Experimentally, the band gap is 5.47 eV and the Young's modulus is 1.1 TPa. Being a relatively simple insulating crystal, diamond was a system of choice for early DFT calculations [20]. The LDA underestimates the band gap, obtaining 4.07 eV for cubic and 3.16 eV for hexagonal diamond, Figure 3.6. According to the LDA, the hexagonal form is 27 meV/atom less stable than the cubic, which is itself 144 meV/atom less stable than graphene.

For the further discussion it is interesting to note that both diamond allotropes have tube-like “tunnels” (Figure 3.6): in cubic diamond, they are similar to (2,2)

²The diamond story is particularly fascinating. Being one of the most famous stones on Earth, it is less known that diamond is also the oldest mineral available to humans. On the basis of the isotopes analysis it has been proven that diamonds are more than 3 billion years old, some of them even up to 5 billion years, older than our own solar system [18]. Most of the natural diamonds we have literally fall from the stars. Although in the Earth's inner core diamonds are also formed, those layers are deep enough that they very rarely find their way to the surface. Almost all available natural diamonds either came as part of meteorites or were formed at the moment of a meteorite impact. Even more intriguing, there is evidence that some white dwarf stars are *themselves* mostly diamonds [19].

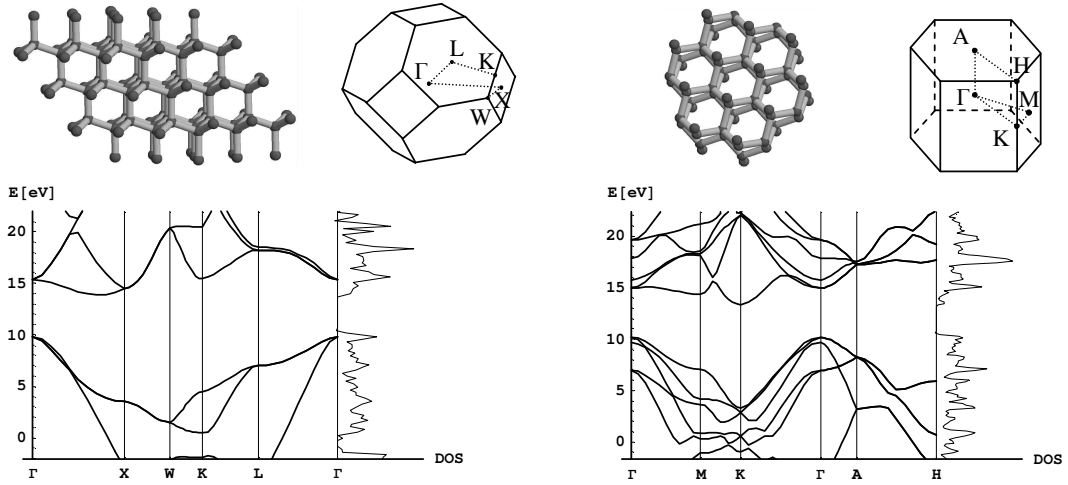


Figure 3.6. Structure, Brillouin zone and LDA bands for cubic (on left) and hexagonal (on right) diamond. The structural images show that the tunnels are similar to the small nanotubes: (3,0) for cubic diamond and (2,2) for hexagonal diamond.

tubes, while in hexagonal diamond they are like (3,0) tubes.

3.2 Novel Carbon Structures

In the last 25 years a series of discoveries [21] showed that carbon can also make stable molecules (fullerenes) and polymers (nanotubes). Moreover, in addition to the earlier known two dimensional graphite and three dimensional diamond forms, carbon can also exist as a disordered sponge-like nanoporous carbon.

3.2.1 Nanotubes

A nanotube is a graphene ribbon rolled in a cylinder with the free edge atoms rebonded in a continuous hexagonal network. Physical properties of such a nanotube depend on the carbon hexagons' orientation relative to the tube's axis. Nanotube nomenclature acknowledges this fact by assigning to each tube two integers (m, n) , which give the orientation of the corresponding ribbon in the graphene plane, Figure 3.7.

Each carbon atom in a tube still has three neighbors as in graphene, but the bonds are slightly off the plane, following the curvature of cylindrical surface. The

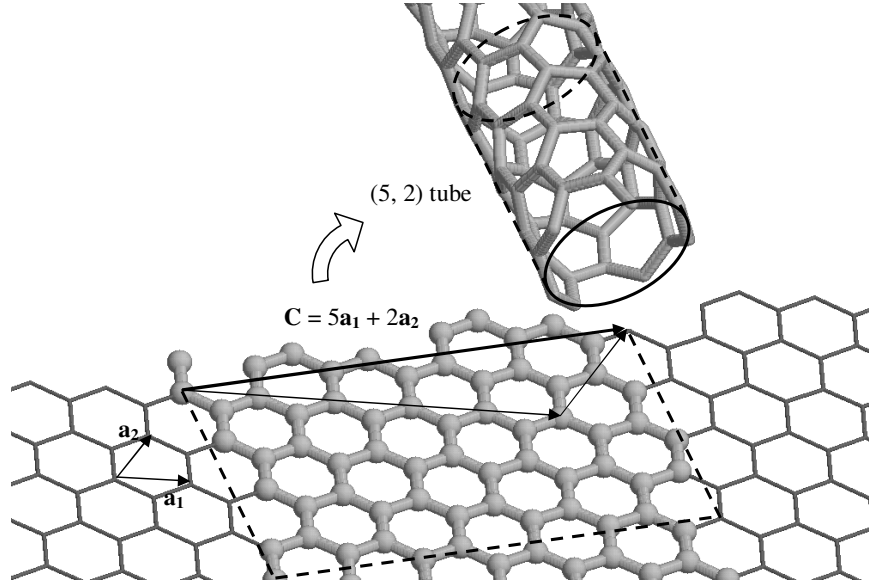


Figure 3.7. Rolling of a nanotube. An unit cell of (5,2) tube is showed unrolled outlined with dashed lines. Unique atoms in the corresponding ribbon are showed as spheres. In agreement with the nanotube's nomenclature, the circumference of the tube corresponds to the vector $\vec{C} = 5\vec{a}_1 + 2\vec{a}_2$ normal to the axis of the ribbon. Vectors \vec{a}_1 and \vec{a}_2 are basis vectors for the translational symmetry of the hexagonal graphene plane, $\|\vec{a}_1\| = \|\vec{a}_2\| = 1.42 \text{ \AA} \cdot \sqrt{3}$.

resulting strain on sp^2 bonds makes tubes less stable than graphene. This effect is stronger in smaller diameter tubes, so that the smallest tubes (less than about 4 \AA in diameter) are not even metastable alone [22]. From the other side, tubes with very big radii are unable to keep a circular cross section and they collapse to two connected graphene ribbons.

Nanotubes are very diverse electronically. Some of them are metals, the others are semiconductors. The simplest way to understand variations in electronic properties of the tubes is to examine what wrapping does to the graphene bands from Figure 3.5. The band folding theory is outlined in Figure 3.8. Only graphene states which can map to themselves around the tube circumference survive the wrapping. That means, the tube states can have only the graphene k -vectors which have component k_\perp normal to the tube axis such that $k_\perp 2\pi R = 2\pi j$, i.e. $k_\perp = j/R$, where j is an integer and R is the tube radius. Thus, in the simplest approximation, one dimensional nanotube bands are slices of the two dimensional graphene bands along a series of equidistant lines. If any of these lines passes through the K point

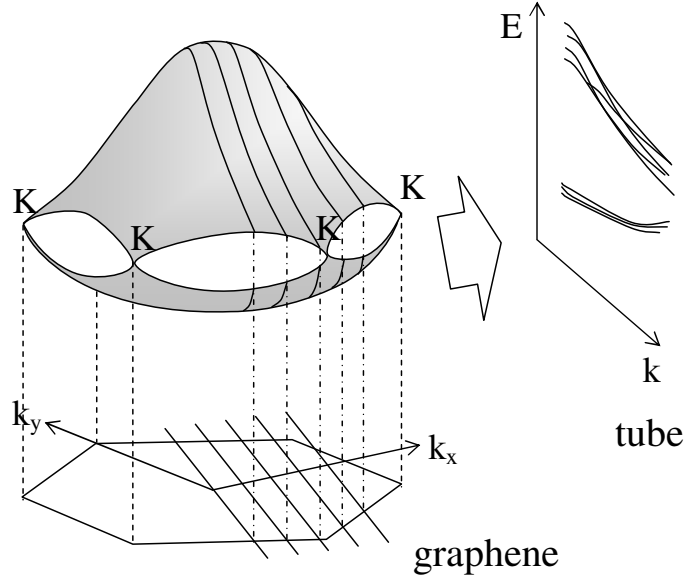


Figure 3.8. The band folding technique forms nanotube bands (shown on right) as combined projection of graphene band slices (lines on the surface), taken across the graphene BZ (hexagon below) along the allowed lines in k-space.

in the graphene BZ, the tube is metallic. A careful calculation [21] shows that this metallic crossing occurs if the tube is of the type (m, n) with $m - n = 3d$, where d is an integer. For example, armchair (n, n) and $(3d, 0)$ zig-zag tubes are metallic, while $(3d - 1, 0)$ and $(3d + 1, 0)$ zig-zag tubes are semiconducting.

Figure 3.9 shows results of LDA calculations for several zig-zag and armchair tubes. The density of states is small around the Fermi level in the metallic tubes. For $(3d, 0)$ tubes the Fermi level wavefunction has $2d$ nodes evenly distributed around the circumference, arranged in lines down the tube. Figure 3.9 shows also that as a consequence of the curvature, π electrons are pushed more toward the outside of the tube.

More precise calculations and experiments show that all metallic tubes except armchair actually have a small curvature-induced gap [23]. For example, “metallic” zig-zag tubes show gaps of up to 80 meV. Since tubes are almost always found in bundles, they interact with each other and in that environment the armchair tubes can also show a small gap.

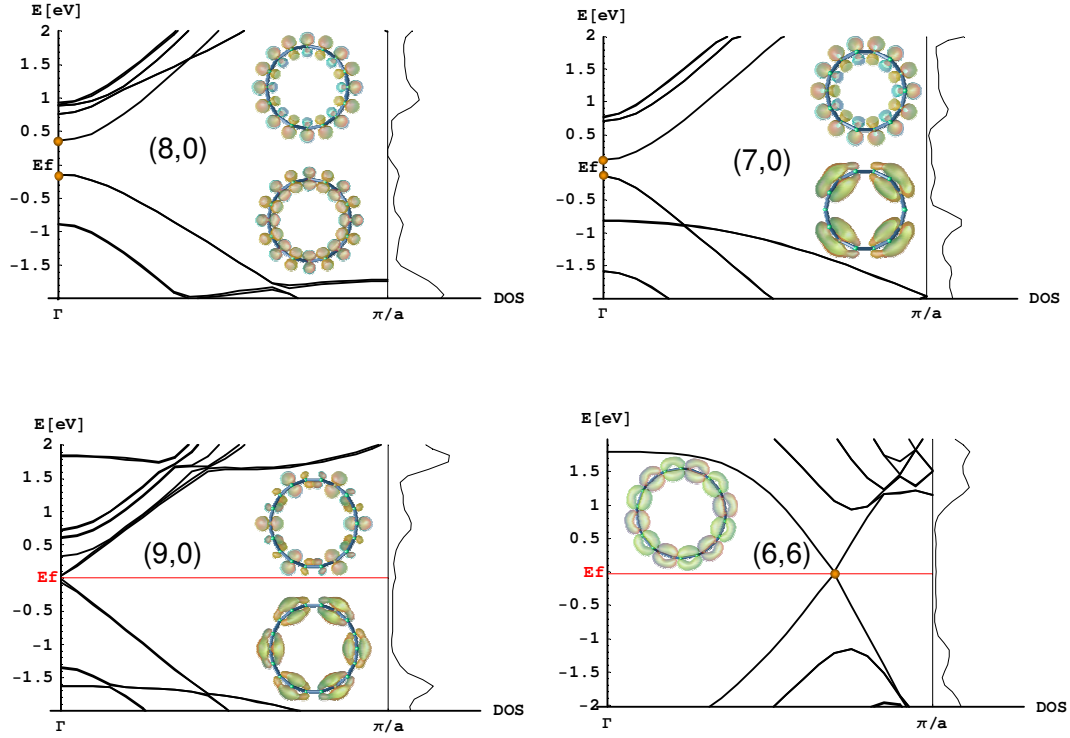


Figure 3.9. Band structure, density of states and partial charge densities for the (7,0), (8,0) and (9,0) zig-zag and the (6,6) armchair tube. Due to the calculation method DOS is smeared by 0.1 eV, so it doesn't vanish sharply at the gap nor it has Van Hove singularities. To show the features, DOS is normalized on each graph and absolute DOS values between tubes might be different. The insets are partial charge densities (equisurfaces for 0.003 \AA^{-3}) from LDA calculations for lowest unoccupied (above) and highest occupied (below) states at the Gamma point. All armchair tubes have similar charge density, while there are three types of zig-zag tubes, two semiconducting and one ($3d, 0$) metallic.

3.2.2 Nanoporous Carbon

Nanoporous carbon (NPC) is a solid microscopically sponge-like material composed mostly of sp^2 hybridized carbon. It has a highly disordered structure with pore sizes around 5-10 Å [24, 25]. This material is quite stable: only after annealing at around 1200°C will its structure start changing, forming graphene-like nanodomains [25].

In equilibrium, the curvature strain is distributed as much as possible equally across sp^2 carbon bonds in NPC. Hence, the idealized structure belongs to the mathematical class of minimal surfaces³ (like a soap film on a distorted frame). The

³Minimal surfaces have mean curvature everywhere zero. Any sufficiently small patch cut

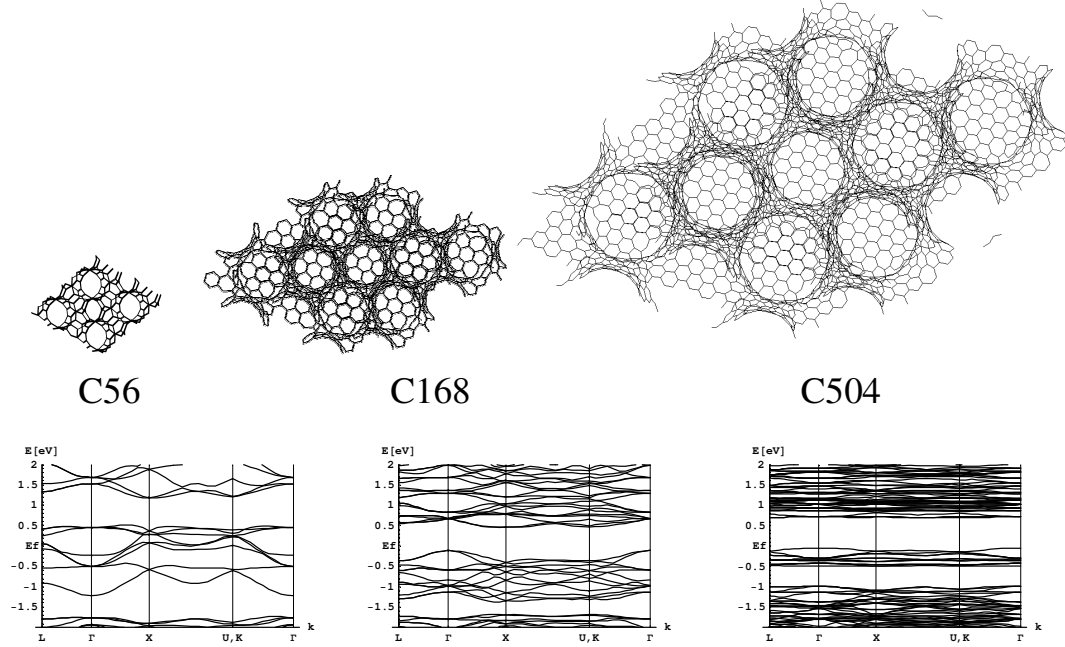


Figure 3.10. $2 \times 2 \times 2$ unit cells and LDA band plots of a series of d-schwarzite carbon structures.

most suitable NPC model for calculations is therefore one of the three dimensional periodic minimal surfaces⁴ first investigated by H. Schwarz [28]. The schwarzites can be tiled with hexagons and heptagons [30] resulting in a highly symmetric sp^2 -only carbon structure.

We have analysed a series of d-schwarzite carbon structures (“d” stands for “diamond-like”, since d-schwarzite has diamond-like space group symmetry) as shown in Figure 3.10. Each of these structures has full tetrahedron point group symmetry [29]. Each successive member of the series is a magnified version of the preceding one, constructed by replacing each atom with a hexagon. This expansion procedure keeps the same number of non-hexagons per unit cell, so that each structure has 24 heptagons per unit cell and the rest are hexagons.

The smallest structure has 56 carbon atoms per unit cell arranged in 24 heptagons. A minimal surface has the least area of all surface patches with the same boundary [26]. Their representations can be found in many physical and chemical systems [27].

⁴“A triply periodic minimal surface is infinitely extending, has one of the crystallographic space groups as its symmetry group and, if it has no self-intersections, it partitions space into two labyrinthine regions. Its topology is characterised by two interpenetrating networks – its ‘labyrinth graphs’” [26].

tagons⁵, without any hexagons. The second has one hexagon between each heptagon, the next has two hexagons between heptagons, etc. Each successive structure has three times as many atoms as the previous one. The pore diameters also increase: 5.4 Å for C56, 6.9 Å for C168, 15.6 Å for C504.

As the unit cell grows in this series, the local curvature decreases. That allows us to isolate effects of global and local geometry on the electronic subsystem.

The bottom part of Figure 3.10 shows bands of this schwarzite series. While our ultrasoft DFT calculations are in agreement with earlier (mostly tight-binding) results [30, 33, 34], there are still no experimental data to compare with, due to the lack of technology which would allow better control of the produced NPC structure. In one of pioneering works on NPC [35] Bursill's group obtained evidence that the NPC band gap is around 2.5 eV.

As Figure 3.10 shows, the smallest (C56) structure is an overlapping band metal. It can be viewed on the same lines as the pentaheptite [36]. Both of these structures have a network of connected heptagons (pentaheptite also has pentagons). Each heptagon introduces one trivalent carbon radical in the otherwise aromatic structure. Radicals consist of π electrons unable to lock in an aromatic resonance [37], leading to the metallic behavior of the overall structure. Chemically speaking, a graphene-like structure has no such radicals, if a global bonding scheme can be found with each tetravalent carbon atom connected to three neighbors by two single and one double bond. Failure to find such a global bonding scheme leads to the introduction of radicals due to a frustration in the electronic system. These radicals are localized in the heptagonal rings where they are formed. However, if heptagons have common edges in the structure, the radicals can overlap leading to a metallic behavior of the overall structure.

The other interesting point from Figure 3.10 is that the band gap increases with the structure size (the gap is 0.72 eV for C168 and 0.75 eV for C504), as opposed to the decrease of the nanotube band gap with increasing radius. This also can be understood on the basis of the heptagonal radicals: the bigger schwarzite structures still have the same number (24) of carbon radicals, but they are spread over a larger number of regular hexagons, so the curvature effect prevails and the gap opens.

⁵On the basis of graph theory [31], 12 heptagons correspond to one hole in a regular graph with three-fold vertices.

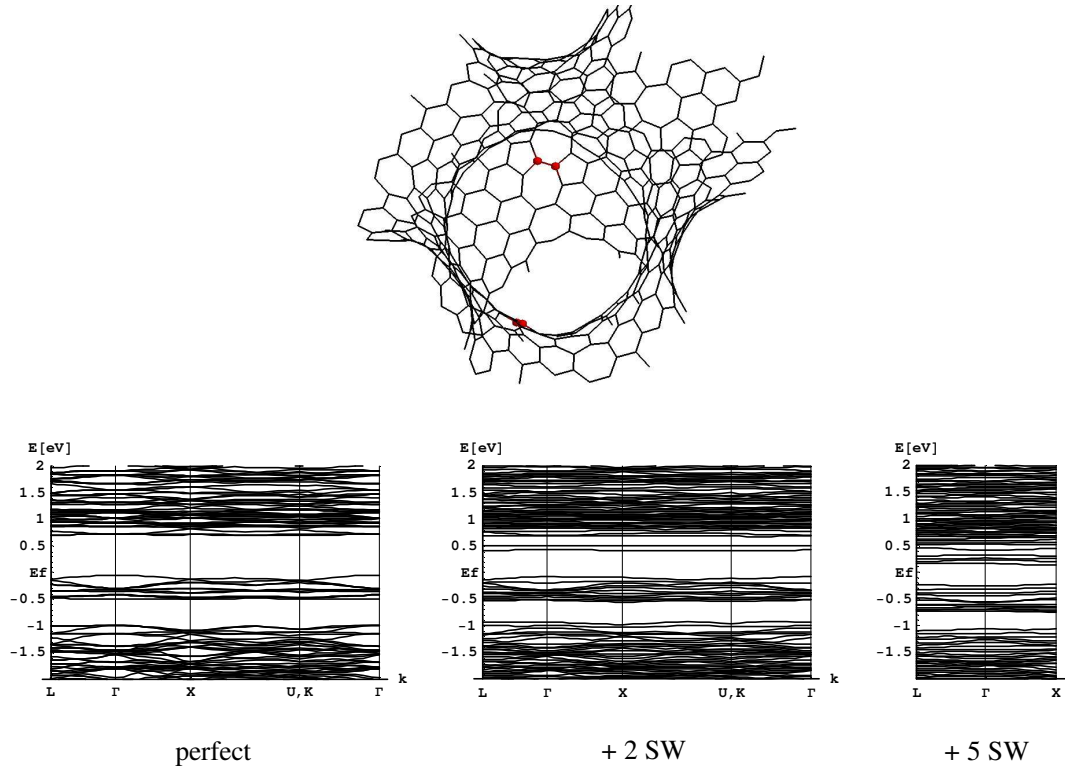


Figure 3.11. LDA band plots of C504 d-schwarzite carbon structure with two and five Stone-Wales defects. SW atoms are emphasized as bigger points in the structural image.

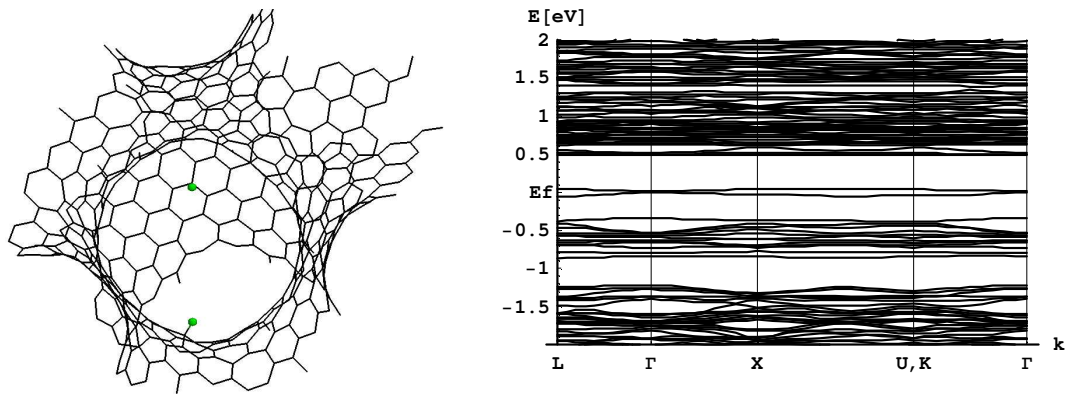


Figure 3.12. LDA band plots of C504 d-schwarzite carbon structure with two chemisorbed hydrogens on the same places where SW defects are in Figure 3.11.

Further, we introduced several distant Stone-Wales (SW) defects [38] in the C504 schwarzite structure, Figure 3.11. The SW defect is a $\pi/2$ carbon-carbon bond rotation. It replaces four adjacent hexagons with two heptagons and two pentagons, introducing two more carbon radicals in the structure. These radicals introduce new bands in the upper part of the gap, so that the gap goes from 0.75 eV down to 0.48 eV for two SW defects and 0.37 eV for five SW defects. Producing more heptagons, SW defects narrow the gap and increase metallicity of the system.

We also compared the effect of SW defects with the hydrogen chemisorption in the C504 schwarzite, Figure 3.12. This is particularly interesting since NPC always contains impurities affecting its properties. Similar to the SW defects, hydrogen introduces additional bands in the gap. Since hydrogen also brings electrons to the system, the Fermi level is raised to an energy between new bands.

The schwarzite calculations presented here illustrate the power of the ultrasoft pseudopotential DFT method, which is the only first-principle method capable of handling such large systems on currently available computers.

Chapter 4

Carbon-Hydrogen Systems

It is interesting how the simplicity of the hydrogen atom also contributes to the complexity of its behavior, which makes hydrogen very different from other elements. Hydrogen can give its only electron and behave as a metal, but also, being one electron short of a closed outer shell, it can produce strong covalent bondings. In elemental form it always exist as a diatomic molecule. Since hydrogen is the simplest atom, the molecule has an exceptionally small bond length of 0.73 Å [39] and is quite stable (the experimental binding energy is 4.52 eV [17], while the DFT estimate is 6.6 eV). It survives to surprisingly high densities in the condensed phase, up to more than 300 GPa [40] but also spontaneously dissociates in the presence of some metallic atoms. The electron wavefunction extent in H₂ is smallest among molecules and hence its van der Waals potential is very weak. For example, the physisorption of H₂ on a graphene surface has a shallow well of 0.08 eV, and an equilibrium distance between H₂ and the graphene surface around 2.7 Å, according to DFT calculations [41].

From the practical side, hydrogen has great energy potential. It has the highest combustion energy on a weight basis among all known fuels. Unlike carbon-based fuels, hydrogen produces no harmful by-products upon combustion. Only clean water is exhausted when hydrogen is combined with oxygen in a fuel cell, generating electricity. Since hydrogen can be produced by the electrolysis of water, it seems as a perfect renewable energy cycle. In practice, however, there are many still unresolved problems in all stages of this loop.

Currently, the technology for powering vehicles (i.e., fuel cells) is significantly

more advanced than that for storing the fuel (hydrogen). One figure of merit for hydrogen storage is the weight percent (wt %) hydrogen stored relative to the weight of the storage medium. The US Department of Energy has recently estimated that approximately 6-7 wt% storage is a benchmark for a viable ground transportation technology [42]. Hydrogen storage in a lightweight carbon material would therefore be particularly attractive¹.

The nanoporous carbon materials like those mentioned in the previous chapter have very high experimental specific surface areas of $A_s \sim 1000 - 3000 \text{ m}^2/\text{g}$ [43]. Despite that, NPC has not shown promise for hydrogen storage [42, 44].

Several recent experiments have reported substantially increased uptake of hydrogen into carbon nanotubes and related structures. The detailed character of the reports is variable, with claims of anomalously high uptake/release of hydrogen at low pressures, high pressures, low temperatures, or high temperatures. The reported uptakes range from single-digit weight percent excess adsorption [45, 46, 47, 49, 51] up to values well in excess of 10% [48, 50]. The highest values, which are unconfirmed (and controversial, [52]), would present a stark challenge to our current understanding of molecular interactions. The more moderate results, which have been verified by gravimetric comparisons of H_2 and D_2 adsorption [53], are still in excess of that expected from standard physisorption.

The unsettled experimental situation suggests that a systematic characterization of the carbon substrate may provide crucial insights. A careful experimental study [54] shows that the wt% hydrogen adsorption depends sensitively on the post-synthesis treatment of the materials. In a companion molecular modeling study presented in the next section we model this process, from post-synthesis treatment to adsorption, through a multistep simulation. First we model annealing of damaged tubes through tight-binding molecular dynamics. We then extract characteristic subunits from these structures for subsequent density functional and diffusion quantum monte carlo analysis of molecular adsorption. The results suggest that microscopic *surface roughening* caused by post-synthesis purification and annealing can help explain enhanced molecular adsorption at anomalously low pressures. The variable and heterogenous nature of this roughening could help

¹Hydrogen interaction with carbon materials plays an important role in a wide range of other problems, from interstellar science [61, 62] to fusion technology [63].

reconcile disparate experimental results, at least at the lower end of the range of anomalously enhanced uptake. This mechanism also implies a well-defined maximal uptake attainable under moderate conditions.

As experiment shows [47], in the high pressure hydrogen storage on carbon nanotubes there is some residual hydrogen during the desorption cycle that could be released only upon heating to temperatures above 400 K. Another experiment [51] revealed a first order phase transition under high H_2 pressure, similar to the hydride phase observed in metal-hydrogen systems. These are all indications that a chemisorption process also plays a role in the hydrogen adsorption on carbon nanotubes. A graphene sheet is well-known to be highly stable against chemisorption of a single hydrogen atom, since a puckered sp^3 hybridized site heavily distorts the surrounding sp^2 framework. However, as we show in section 4.2, successive adjacent chemisorbed hydrogen atoms can engage in a collective stabilization mediated by cooperative alternate puckering in the underlying carbon sheet [55]. After several chemisorbed atoms, the binding energy for further adsorption changes sign and becomes favorable. This process requires access to both sides of the graphene sheet. Therefore it is suppressed on a graphite surface, but may be accessible in carbon nanotubes, if the initial kinetic barrier to creating the nucleation island can be overcome.

Hydrogen chemisorption can be also used to engineer new carbon-based materials with unique structural and electronic properties. In section 4.3 we describe how sp^2 carbon, three-fold coordinated to other carbons, can be replaced by sp^3 carbon, also three-fold carbon coordinated, to produce extremely small-radius ($\sim 0.4nm$) carbon nanowires with minimal bond-angle distortion. Such systems would be extremely small-diameter, robust and rigid one-dimensional atomic structures [56]. Following an analogous naming convention for ordinary carbon-nanotubes, the most stable sp^3 tubes are the (3,0) and the (2,2) tubes, which we examine in detail. These high symmetric systems have a large bandgap typical of saturated hydrocarbons and a huge rigidity.

Finally, in section 4.4 we show how conversion of two diametrically opposite rows of atoms on a carbon nanotube into sp^3 hybridization through hydrogen chemisorption have huge effects on the nanotubes electronic structure [57]. Particularly, the armchair tubes undergo an effective separation into two weakly interact-

ing metallic wires, resulting in a pair of very narrow bands near the Fermi energy. Although this system has an even number of electrons, energies of electronic states near the Fermi level are so close that the ground state stabilizes in a magnetic state with two top valence bands half filled with the same spin electrons. If the system is doped with electrons or holes, or spin flip is allowed, these tubes could be very active terahertz materials with an exceptionally high joint density of states, as well as a high polarizability. We propose that in experiment a uniaxial compression of a nanotube transverse to the axis could enable adsorption preferentially in the required pattern.

4.1 Hydrogen Physisorption on Tubes

Arc-grown nanotube samples are typically purified via aggressive acid or oxidative treatment. This treatment selectively destroys the less resistant carbon and metallic impurities, but also eats away at the walls of the tubes themselves. The treatment produces a wide distribution of holes and defects in the tube walls which can yield a “dog-chewed” morphology. A recent experiment by the Penn State group [54] suggests that a high temperature post-treatment anneal is critical to optimizing the hydrogen adsorption at low pressures. During this anneal the nanotube partially heals the holes that were created by the acid treatment. Due to limited carbon mobility and structural constraints arising from intact subregions of the tubes which maintain circumference integrity, only incomplete healing is possible and the resulting surface is of necessity irregular on a nanometer scale.

Such structures exhibit two important new structural features. First, the tiny (and strongly hydrogen-binding) interstitial channels of the pristine bundle open into wider intertube galleries. Second, atom transport during the healing process must of geometric necessity produce many pentagonal and heptagonal carbon rings; pentagon rings are particularly favored as they most efficiently saturate the dangling bonds at the edges of the holes. Both the enlarged interstitial galleries and the roughened tube surfaces can significantly increase the low-pressure binding of molecular hydrogen, as described below.

The trigonal interstitial channels within intact (i.e. defect-free) nanotube bundles of typical tube diameter (circa 1.4 nm) are very strongly binding for hydrogen,

with binding energies roughly two to three times that of a graphene sheet (as would be expected from a simple coordination number estimate). Unfortunately, these sites comprise very little free volume; most of the outer surface of the tubes interior to a bundle is wasted. However, the interstitial region is so small in intact bundles only because perfectly cylindrical structures of uniform diameter can pack very efficiently. The irregularities in tube shape resulting from partial healing of damaged tubes can open up a much greater volume of high-coordination (and therefore highly binding) interstitial sites. Hydrogen within these enlarged interstitial galleries will be coordinated to either one, two, or three adjacent graphitic sheets, depending on the local geometry. Therefore the enhancement in the hydrogen binding energy above that of a free graphene surface (circa 0.05 to 0.07 eV) will range upward from one-fold to roughly three-fold, within the range necessary to account for cryogenic adsorption at the observed low pressures.

A roughened graphitic surface may exhibit a more subtle enhancement in adsorption arising from pervasive distortions in local bonding. We model adsorption onto disordered graphene-like structures by generating candidate structures and studying the subtle differences in hydrogen-binding energy to their surfaces. Figure 4.1a shows the result of a tight-binding molecular dynamics [4, 58] simulation of a defective (8,8) nanotube. Ten percent of the atoms were first removed in random patches from a pristine (8,8) structure. The system was then annealed at 2500K (artificially high) for 0.5 ps and then cooled to the local equilibrium structure over 1.5 ps using a time increment of 0.5 fs and a canonical-ensemble Nosé-Hoover thermostat with a mass of 50000 a.u.

The tube has found a very efficient means to self-bind, returning to a state near its global structural ground state and healing most of its holes by introducing irregularities, mostly five and seven rings. A cross-sectional view shows strong deviations from circularity. We characterize the distortion from local planarity by the deficit of the summed local C–C–C bond angles from 360° , as shown in Figure 4.1. The most curved regions correspond to the sites where the anneal produces fused pentagons. They have the summed bond angle deficit of 15 degrees, comparable to those obtained in fullerenes of fewer than 60 carbons. Figure 4.1b depicts a bundle of seven such tubes to demonstrate how the roughening of the tube surfaces enlarge the interstitial channels. These seven tubes were relaxed

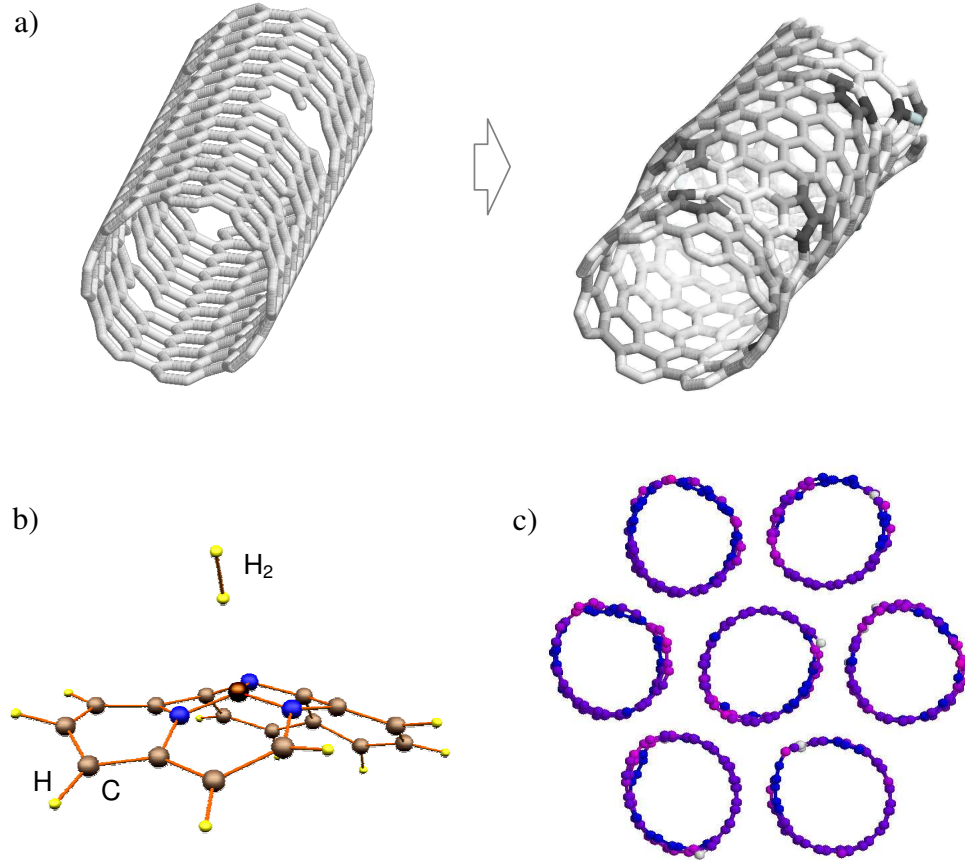


Figure 4.1. (a) The starting structure, an (8,8) tube with 10% atoms removed and computed nanotube structure with rough walls obtained from simulation of a rapid high-temperature anneal of a damaged tube, as described in the text. Darker carbon atoms exhibit larger deviations from planarity, showing that the distortions propagate outward from pentagonal rings. The darkest region has summed bond angle deficit of 15 degrees on a site between two fused pentagons. A patch with two fused pentagons extracted from such a nanotube is shown in (b), provided courtesy of Jeffrey Grossman, with the relaxed position of a hydrogen molecule above the most distorted carbon atom. The seven-tube bundle shown in cross section in (c) is built from the same tube, but each replica has a random orientation and was allowed to relax to an intertube separation dictated by a standard intertube van der Waals interaction.

as individual rigid objects into a bundle geometry via intertube Van der Waals interactions. We believe that the relaxation of the internal coordinates within a tube would have increased the interfacial contact area only slightly.

The experimental purification can range widely in aggressiveness and the anneal can likewise cover a wide range of temperatures and timescales, so the microstruc-

ture is expected to vary widely from experiment to experiment as treatment and anneal conditions are changed. In addition, the molecular dynamics can address the system evolution only over short time scales (even when the temperature is artificially elevated, as is often done to speed the dynamics). Thus, the structure resulting from our molecular simulation should be viewed as illustrative rather than definitive. However, we consider the molecular dynamics simulations to produce particular examples of physically realizable local structural motifs that are attainable experimentally in varying concentrations depending on the particular experimental history of the sample.

Since tight binding models cannot describe the subtle mixture of dispersion and hybridization involved in the interaction of molecular hydrogen with a heavily distorted carbon substrate, we extract characteristic local regions from the molecular dynamics and input them to LDA DFT and diffusion Monte Carlo (DMC) calculations of hydrogen physisorption (this was done in collaboration with Peihong Zhang for LDA calculations and Jeffrey Grossman for DMC calculations). The outer edges of these extracted patches are terminated with hydrogen to eliminate unsaturated bonds, but the outer regions of the structure, away from the adsorbed hydrogen, are maintained rigid to preserve the overall roughness. Since the experimental structure is highly disordered, we have studied a range of relevant local structure motifs: (1) a 20-atom section showed on Figure 4.1b with two fused pentagon rings extracted from a disordered tube such as Figure 4.1a and capped at the edges by hydrogen atoms, (2) a 16-carbon atom planar molecule comprising four fused hexagonal rings (denoted “6666”), and (3) a series of distorted 14-carbon aromatic molecules composed of two hexagons and two pentagons fused (“5665”). The atomic coordinates within the 20-atom extracted patch are maintained at the positions assumed when embedded in the larger system. The 6666 molecule was fully relaxed; the 5665 series covered a range of deviations from planarity to investigate the heterogeneity of a roughened tube. In each case, we place a hydrogen molecule above the center of the patch and allow the adsorbate to relax. (We also tested several different starting positions for the hydrogen molecule to more thoroughly explore possible resting positions.) The specific value of the binding energy obtained is a complex function of the local bond angles, ring structure, and external strain. The 6666 system, which models a flat undistorted graphitic sheet,

shows a binding energy within LDA of 0.072 eV, consistent with previous results for adsorption on graphitic sheets [30]. Both the 5665 series and the extracted patch show substantially increased adsorption energies: from 0.087 to 0.092 eV for the 5665 series and 0.095 eV for the extracted patch.

To obtain an accurate measure of the actual enhancement, these preliminary values must be corrected for the well-known LDA overbinding of weakly bound molecular systems. To this end, we have computed accurate first-principles DMC energetics for a system of three fused pentagons, obtaining 0.09 and 0.07(1) eV in LDA and DMC, respectively. The characteristic LDA overbinding in this case is moderate (approximately 20 meV), which lends confidence to the overall picture. With application of an approximately 20 meV overbinding correction, the adjusted binding energies range from approximately 52 meV (in DMC-corrected 6666) to approximately 75 meV (in the DMC-corrected 20-atom patch from the disordered tube). The computed enhancement in binding energy due to surface roughening is found to be quite substantial, i.e. 40-50%. The local roughening seems to affect the hydrogen binding through a complex interplay of aromaticity, bond distortion and local coordination.

These results reveal an intimate connection between an enhanced adsorption and structural metastability due to distortions arising from nanometer-scale structural constraints. A larger adsorption energy may occur in structures wherein the carbon substrate is unable to fully accrue the energetic advantages of self-binding. Our calculations suggest that the aggressive HNO_3 treatment pushes the material far from structural equilibrium by creating large holes in the tube walls. Partial healing during the subsequent anneal then spreads this disequilibrium more evenly throughout the structure and could yield a substrate with enhanced physisorption at low pressure, if the roughening is sufficiently pervasive. Note that the physisorption energy increases even though the carbon coordination of a hydrogen molecule decreases due to the local convexity of the carbon sheet. This bodes well for hydrogen storage, since higher binding at lower coordination to the substrate implies a greater overall efficiency in creating favorable adsorption sites within the structure. Other disorder-induced effects, as improved access to the high-coordination concave interior surfaces contribute to even bigger H_2 adsorption.

4.2 Hydrogen Chemisorption on Tubes

The similar energies of different hybridized states of carbon lead to its versatile chemical behavior. Graphite and nanotubes, as two elemental forms of carbon, demonstrate this flexibility through their ability to make new chemical bonds with chemisorbed atoms while preserving the original carbon hexagonal net. One important case in which this happens is hydrogen chemisorption. A review of recent chemisorption calculations can be found in [60]. Nanotubes with ordered outside chemisorbed hydrogen is considered in [65, 66]. In [67] a combined classical/quantum mechanical study is presented, where only tube region around chemisorbing site is treated quantum mechanically. Hydrogen chemisorbed from inside and outside of the tube was analysed in [68]. Here we focus on the strong variations of the energy of chemisorption as a function of the hydrogen coverage.

Although catalysts such as Pt on graphite can dissociate H_2 molecules and place atomic hydrogen in contact with graphite, a defect-free graphene basal plane is highly resistant to chemical attack by free hydrogen atoms. Not only is the kinetic barrier to hydrogen chemisorption generally large, but an isolated hydrogen atom sp^3 bonded to a graphene plane is also energetically unfavorable compared to the clean graphene sheet plus the same hydrogen in the (molecular) gas phase [62]. However, the binding of an isolated hydrogen atom onto a clean and defect-free graphite basal plane does not provide a complete picture of the pathways towards a fully hydrogenated carbon sheet. An sp^3 coordinated carbon atom within a graphene layer imposes a strong pattern of buckling on the surrounding atoms; the buckling patterns from nearby sp^3 atoms can overlap and possibly reinforce. Such a collective stabilization, favoring successive hydrogen addition, is distinct from the well-known effects of broken aromaticity in hydrogenating small molecules. For example, in the conversion of benzene to cyclohexane, the first hydrogen attachment is most costly, since it breaks the π ring conjugation; later hydrogens are easier to attach. In a small molecule like benzene, the bond angles can adjust relatively freely to accommodate nearby sp^2 and sp^3 atoms. In contrast, an extended graphene sheet imposes strong elastic constraints that create a frustrated sp^3 -like buckling around a single chemisorbed hydrogen. However, if chemical attachment is possible on both sides of the graphene layer, then

these local bucklings can reinforce each other. This cooperative sheet-mediated adsorbate-adsorbate interaction can change the sign of the adsorption energetics, making further chemisorption energetically favorable. For comparison, note that graphite surface has been fluorinated, converting the sp^2 network largely to sp^3 , since the F_2 molecule is highly reactive, as experiments on graphite [72] and on tubes [69, 70, 71] as well as calculations [65] show.

Unlike hydrogen physisorption (section 4.1), which involves subtle many-body van der Waals effects, hydrogen chemisorption can be well described by standard semiempirical and density functional methods. However, in order to accurately describe collective effects, large systems must be simulated. Therefore, we first employ a focussed set of density functional theory (DFT) calculations to validate further use of more computationally efficient empirical tight-binding total-energy methods [4] for a much larger set of complex multi-adsorbate geometries.

The total energies for each configuration with chemisorbed hydrogen are compared to those of a suitable reference structure, namely a pure-carbon pure- sp^2 structure plus the same hydrogen atoms in isolated hydrogen molecules:

$$\Delta E = E - E_0 - \frac{N_H}{2} E_{H_2}, \quad (4.1)$$

where N_H is the number of attached hydrogens, E is the total energy of the configuration in question, E_0 is the energy of the pristine pure- sp^2 pure-carbon system and E_{H_2} is the energy of a single hydrogen molecule. Negative ΔE corresponds to energetically favorable adsorption. It can be divided by N_H to obtain a binding energy per hydrogen atom. Vibrational entropy will favor hydrogen geometries with weaker bonds, but this effect should not disrupt the overall energetic trend towards cooperative adsorption. Since we focus on relative energetics, we do not consider vibrational entropies or pressure-dependent gas-phase entropic terms. This treatment differs from previous studies [66, 73], in that we compare the bound system to a clean substrate plus molecular rather than atomic hydrogen.

An isolated chemisorbed hydrogen induces a local distortion of the surrounding carbon atoms, creating an intermediate sp^2/sp^3 bonding character on neighboring atoms. This distortion induces a slight dangling bond character in its immediate neighborhood and affects the energetics and kinetics for adsorption of additional

hydrogen. The most favorable site for successive hydrogen addition should generally be immediately adjacent to the existing cluster, at the point with maximal bonding distortion. The number of possible arrangements of nearby adsorbed hydrogens grows roughly exponentially as the number of hydrogen atoms increases. Therefore, instead of exhaustively analyzing all possible configurations for a given N_H , we start from $N_H = 1$ and construct successively larger clusters by following the lowest-energy pathway for successive hydrogen addition. For small or linear clusters this strategy requires evaluation of $\sim N_H$ structures, since roughly half of the possible cluster edge sites are equivalent. For big compact clusters, evaluation of $\sim \sqrt{N_H}$ structures is enough at each stage, since every site near the perimeter of the N_H configuration must be tested to determine the most favorable $N_H + 1$ configuration.

We examine three different stages with successively higher hydrogen densities: (1) the beginnings of chemisorption, wherein a small number of hydrogen atoms attach to a graphene surface in a local cluster, (2) the extension of an adsorbed state along a tube axis, using high-symmetry configurations to simplify interpretation and (3) the hydrogenation of the last few remaining sp^2 carbon atoms in an almost fully hydrogenated sheet-like carbon structure.

To examine the initiation of chemisorption onto an (8,8) carbon nanotube, we use VASP [74] package to make a series of local density approximation (LDA) density functional theory (DFT) calculations with ultrasoft pseudopotentials and a 300 eV plane wave energy cutoff. We use a supercell containing 3 unit cells of the (8,8) tube (with total 96 carbon atoms) to adequately isolate the clusters of attached hydrogens in each repeated unit. Since the chemisorbed patches are well separated, the simulations use only the Γ ($\vec{k} = 0$) point. The supercell has dimensions of $21 \text{ \AA} \times 21 \text{ \AA} \times a_z$, where $a_z \approx 7.3 \text{ \AA}$ varies between structures, since the system is fully relaxed along the z direction. The ionic relaxation has been carried on up to the point when the relative total energy change is less than $1.0 \cdot 10^{-4}$ per unit cell.

The tight binding calculations for the same supercell structures have been made within a nonorthogonal tight-binding scheme [4] implemented in program Trocadero [75]. In this calculation a structure has been considered relaxed when the relative total energy change becomes lower than $0.2 \cdot 10^{-4}$. In every case, the

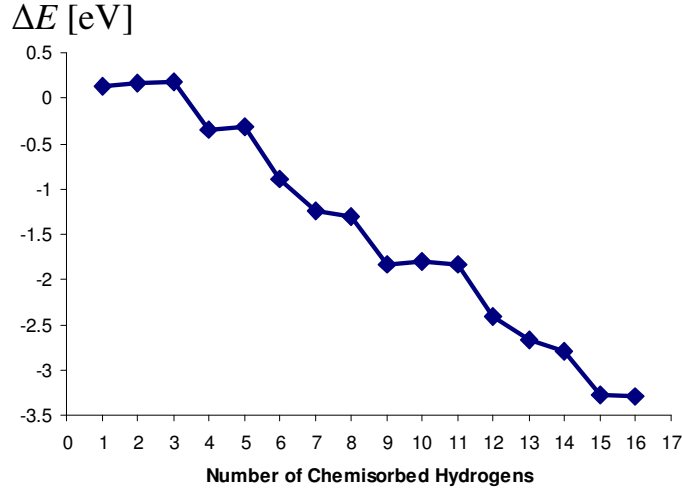


Figure 4.2. LDA DFT results for the energy ΔE of the hydrogen chemisorption on the (8,8) tube, following the minimal energy path described in the main text.

structure is fully relaxed into the local energetic minimum.

Figure 4.2 shows relative total energies ΔE for a growing hydrogen cluster with atoms attached to both sides of an (8,8) nanotube, calculated using spin polarized LDA DFT. The smallest chemisorbed clusters are unstable, but at $N_H = 4$ the chemisorbed state becomes energetically favorable. This behavior manifests as a collective reinforcement of the buckled sp^3 network. As a consequence of the wall curvature, the cluster grows further with hydrogen arranged in an armchair circumferential row, with more hydrogens on the outside than on the inside surface (Figures 4.4 and 4.5).

Unlike most chemisorbed or physisorbed systems, which have a relatively weak density-dependent binding energy, the binding energy for hydrogen chemisorption in this case is highly density-dependent and even changes sign. The explanation for this distinction is two-fold. First, carbon is nearly isoenergetic in two very different bonding geometries, so that the chemisorption process is accompanied by a large change in local bond angles. Second, the graphene substrate is a single two-dimensional atomic layer, rather than the surface of a three-dimensional solid. This very thin substrate is then susceptible to buckling distortions perpendicular to the plane and, unlike bulk graphite, atoms can attach to both sides.

Next we calculate the same series of structures using the tight binding total

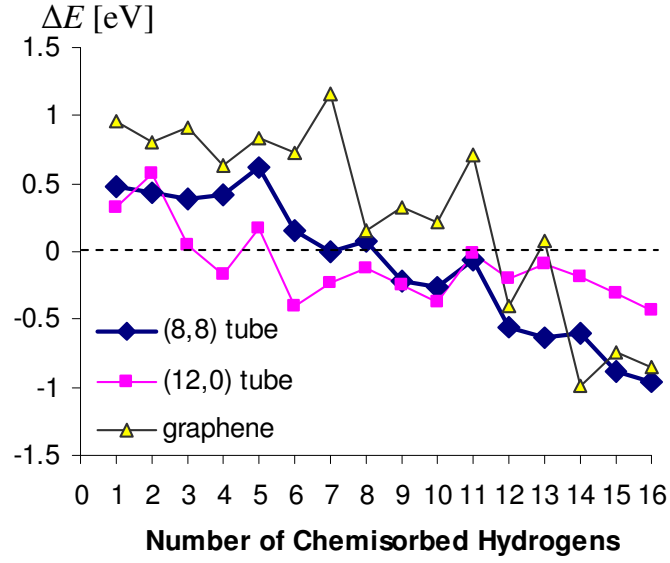


Figure 4.3. Tight binding total energy difference ΔE of hydrogen chemisorption following the minimal energy path, as described in the main text. Configurations with negative ΔE are more stable than a corresponding clean carbon structure plus molecular hydrogen.

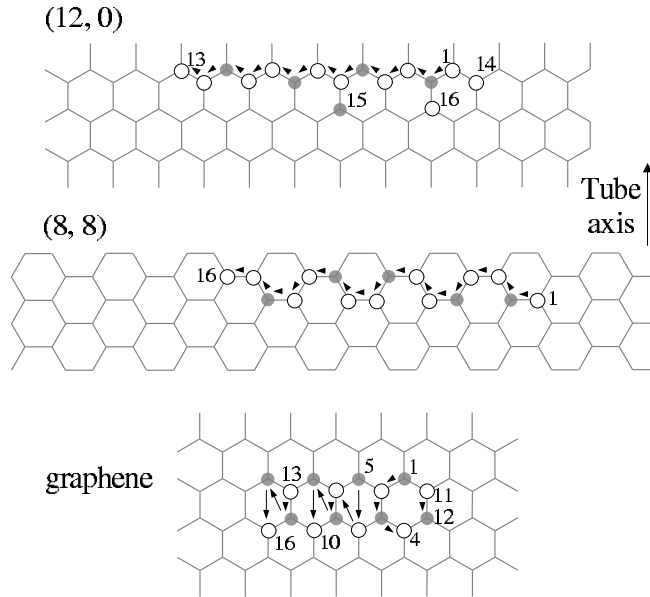


Figure 4.4. Sequences of hydrogen atoms chemisorbed by following a minimal energy path for the (8,8) and (12,0) tubes and graphene. Gray disks represent atoms chemisorbed inside the tube or below the sheet. Arrows show the path of successive hydrogen addition. Hydrogen atoms with explicit index numbers are discontinuities in the path.

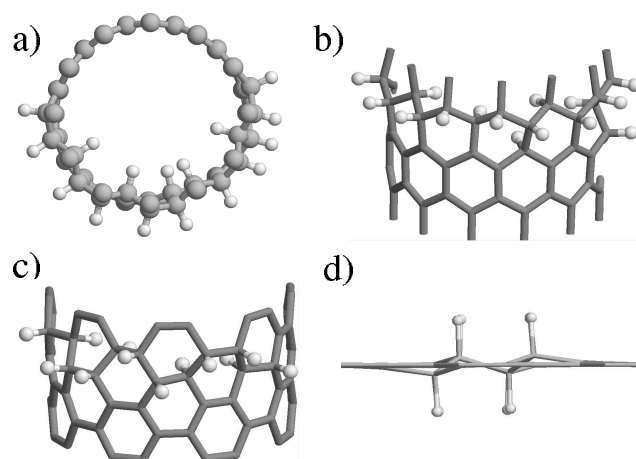


Figure 4.5. The final configurations of a sequence of hydrogen atoms chemisorbed by following a minimal energy path. (a) On the smaller-diameter (12,0) tube, the strain on the clean part of the tube induces a new row ((b), side view) to start before the first row circles the belly of the tube. (c) In the (8,8) tube, the cluster again grows as a ring around the circumference. (d) In the graphene sheet, hydrogen atoms arrange in a double zig-zag row. The edge-on view for the graphene sheet emphasizes the sp^3 -like vertical distortions away from the perfectly planar sp^2 starting structure. Schematic top views of the same structures are shown in Figure 4.4.

energy approximation. The result (black diamonds on Figure 4.3) shows the same trend as the DFT result, Figure 4.2, but shifted upwards and with a somewhat smaller slope (possibly due to an underestimate of longer-range energetic contributions from broken aromaticity). Both curves have peaks and valleys with similar locations, except on the beginning of the chemisorption process, where tight binding underestimates the graphene resistance to the first hydrogenization and then show a rather slow change in the cluster stability, predicting the first stable cluster only after 9 hydrogens. In addition, the tight-binding-based minimal energy sequence yields the same shape for the optimal sixteen-atom hydrogen cluster: an armchair row around the tube. This comparison shows the tight binding total energy method is reasonably accurate for carbon in the vicinity of sp^2 and sp^3 bonding geometries, and so should be able to describe the main features of cooperative interactions between nearby adsorbates, especially in advanced cluster growing.

Since tight binding gives the correct trend for the total energy of hydrogen chemisorption, we next use it in a comparative study of hydrogen chemisorption

onto three different systems: the tripled unit cell (8,8) nanotube already mentioned, a doubled unit cell (12,0) tube, also with 96 carbon atoms, and a flat defect-free single graphene sheet with 384 carbon atoms (but roughly the same unit cell volume as for the tubes). The flat graphene sheet, when compared to the tube systems, reveals the effects of wall curvature and bond orientation relative to the principal axes of curvature. In each case, we assume that atomic hydrogen has access to both sides of the carbon surface, as would be the case for a nanotube with open ends or sidewalls [76].

Figure 4.3 shows the tight binding energies ΔE for growing clusters. The smallest chemisorbed clusters are again unfavorable, but at $N_H \approx 6 - 10$ the chemisorbed state becomes energetically favorable on all three structures. The minimal stable cluster is smaller when the curvature of the underlying carbon net is bigger, since sp^3 bonding angles for outwardly-attached atoms are more easily fit onto a curved surface and the system can adjust the relative numbers of inside and outside hydrogen atoms.

In each case, the patches of hydrogen are most stable as a double row of adsorbed atoms [67] (see Figures 4.4 and 4.5). For the flat sheet, this double row follows the so-called zig-zag direction of the graphene lattice. As a consequence of wall curvature, both nanotubes favor hydrogen arranged along a circumferential path, even though the (n,0) and (n,n) tubes have quite different bond orientations relative to the tube axis. The small diameter of the (12,0) tube cannot easily support an sp^3 state with equal numbers of hydrogens on the outside and inside: the inside hydrogens are less compatible with the overall wall curvature. Therefore, a second row starts before the first row is complete, similar to what happens for intermediate sized pure- sp^3 tubes [56]. For larger radii the curvature is less important and hydrogen atoms can complete a ring before the next row begins.

The above presented results suggest that progressive hydrogenation would proceed in a row by row fashion, as has been found experimentally for fluorinated systems [69]. Verifying this model in detail is not a simple task, since cluster formation becomes harder to follow step-by-step as the number of hydrogen atoms increases. Instead, we model further growth by restricting attention to a set of high-symmetry structures with hydrogen atoms arranged in a series of rings around the (8,8) and the (12,0) tubes. The small clusters already show that not all hydrogen

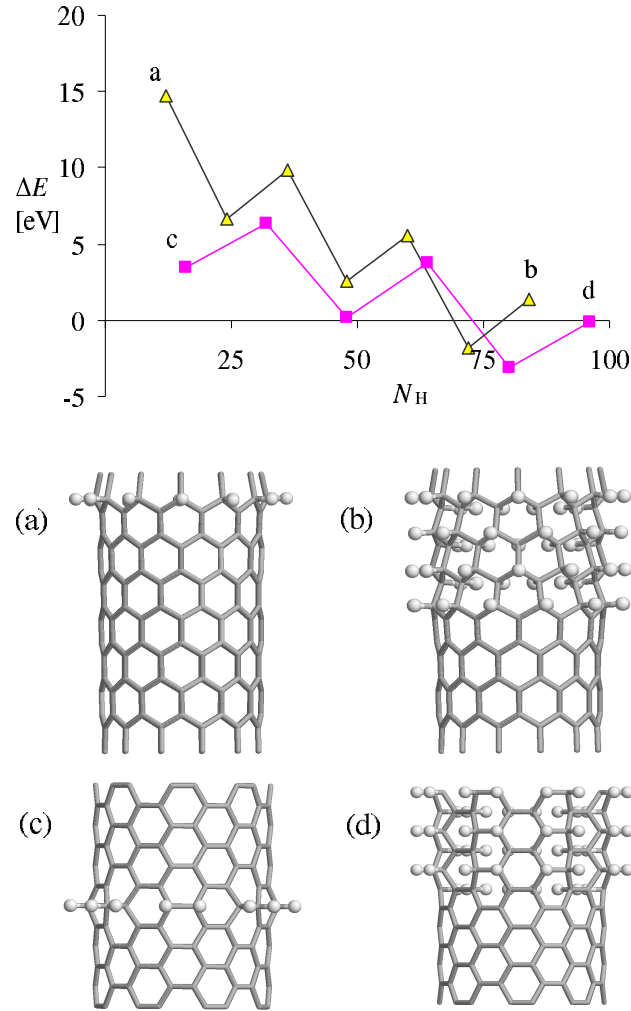


Figure 4.6. Difference in the energies ΔE for (8,8) (squares) and (12,0) (triangles) tubes with completed rows of chemisorbed hydrogen. Rows alternate from the outside to the inside of the tube. Four structures (a-d) are detailed in the text.

atoms in one row should be on the same side of the tube, so these structures are not energetically the most favorable, but they provide a simple view of possible modes of propagation for an adsorption front along the axis of the tube.

Figure 4.6 shows the energy difference ΔE for successive row-by-row adsorption. In order to avoid interaction between images, these tight binding calculations use larger supercells with 192 carbon atoms. The outside (represented in the text as \uparrow) and inside (\downarrow) hydrogen rings alternate, following by the unhydrogenated ($-$) carbon sp^2 rings. Since the atoms in each ring are equivalent, corresponding

structures can be labeled using their cross sectional shape. The figure contains models for the first configuration, ($\uparrow - - - - -$), containing just one hydrogen row attached on the outside surface and two later configurations: ($\uparrow\downarrow\uparrow\downarrow - - - - -$) for the (8,8) tube (with six filled rows) and ($\uparrow\downarrow\uparrow\downarrow\uparrow - - - - -$) for (12,0) tube (with seven filled rows).

Energies for the higher-symmetry row-by-row filling are higher than those for the small clusters, as expected. The axial propagation of the chemisorbed state favors addition of rows in pairs, rather than sequentially row-by-row, since the distortion of the remaining sp^2 part is then minimized and the sp^3 atoms interior to the patch maintain a consistent geometry. The reduction in the total energy per hydrogen atom after each ($\uparrow\downarrow$) step is $\Delta E/N_H \approx -100\text{ meV}$ for the (8,8) tube and $\Delta E/N_H \approx -180\text{ meV}$ for the (12,0) tube. Similar to the initiation of chemisorption, the total energy ΔE decreases and the overall process is self-propagating in an energetic sense. As a consequence of different carbon bond orientations, the armchair (8,8) tube prefers configurations with one extra row on the outside, while the zig-zag (12,0) tube prefers equal numbers of inside and outside rows. In larger systems, antiphase boundaries between different domains could introduce frustration into the pattern of buckling at the boundaries.

The linear scaling of the total energy gain with respect to the number of chemisorbed hydrogens in the row-by-row cluster propagation shows that the energy gain when two hydrogen belts are added is independent of the cluster size (except in the beginning of the chemisorption process, i.e. near the origin in Figure 4.6, which always must belong to the curve). This is possible only if the collective stabilization of chemisorbed hydrogens has a relatively local character, so that in the cluster all interior atoms give the same contribution to the cluster energy.

Finally we consider the other extreme of hydrogen chemisorption, a tube completely filled with hydrogen. This is a complement to the clean tube, being again a uniform tubular structure, but built with sp^3 instead of sp^2 carbon. For each sp^2 -tube there is its sp^3 carbon-hydrogen counterpart (section 4.3). These structures are significantly more stable than their sp^2 twins (plus gaseous hydrogen). For example, the (8,8) sp^3 tube is 140 meV per hydrogen atom more stable than its sp^2 counterpart, while the (12,0) tube is preferred by 233 meV per hydrogen. The final steps of adsorption just before attaining complete sp^3 coverage perhaps

most strongly demonstrate the importance of the collective stabilization. It is simplest to examine this limit by working backwards and considering the removal of a succession of hydrogen atoms from a saturated tube. The sp^3 (8,8) tube with 96 carbon atoms and a single missing hydrogen atom is already ~ 1.9 eV (in tight binding) less stable than the saturated tube. Therefore the reverse reaction, i.e. the completion of saturation, is highly favorable. The second and third hydrogen atom can be detached from nearby sites in a several different ways, but they all have similar total energy cost of about ~ 1.5 eV, within the same empirical approximation.

The resistance of a pristine graphite basal plane to attack by atomic hydrogen has two distinct kinetic barriers: the familiar “local” barrier against changing the bond hybridization of a specific carbon atom and also a more collective “global” nucleation barrier, wherein a finite number of adjacent hydrogens must be attached before the addition of subsequent hydrogens becomes energetically favorable. The kinetic barrier against this self-reinforcing process is substantial. Methods to overcome this nucleation barrier could include the creation of defects in the sp^2 sheet, the incorporation of pre-configured small hydrocarbons that built-in the structure of a seed cluster, or initial fluorination of the sheet, followed by a concerted exchange of fluorine for hydrogen. Single-walled carbon nanotubes seem a particularly favorable substrate for this behavior, since both sides of the sp^2 surface are potentially accessible and the wall curvature reduces the size of the critical cluster. One possible source of the atomic hydrogen needed is a dispersion of nanoparticulate Pt catalyst. The local kinetic barrier against chemisorption is much smaller for the atomic hydrogen (0.3 eV) than for molecular hydrogen (around 3 eV) [77]. This barrier may decrease further with progressive buckling of the carbon surface, since potential host carbons adjacent to the current cluster deviate more strongly towards an incipient sp^3 dangling bond structure under the influence of the collective sheet distortions.

We simulated the chemisorption of hydrogen on bilateral carbon surfaces, allowing hydrogen to access the both sides. In simulations we used DFT and semi-empirical tight binding methods. We justified the tight binding results comparing them with DFT in one system and then we used it to compare hydrogen chemisorption on a typical zig-zag, armchair tube and the graphene sheet. In each of these

cases hydrogen cluster becomes favorable after some initial size. On tubes it prefers to grow as a belt, in a row-by-row manner, so we modeled the cluster’s further extension comparing a series of well ordered structures, with hydrogen atoms arranged in rows around the tube. This system gains energy if the rows are added in pairs, one from the bottom and one from the top of the tube. Next, we discussed the other end of the chemisorption process, the sp^3 CH tubes. We found they are very stable structures. Finally, we discussed possible experimental realizations of the modeled systems and proposed methods to overcome the cluster nucleation barrier.

4.3 Carbon-Hydrogen sp^3 Tubes

The atomically thin two-dimensional covalent structure of a graphene sheet can be distorted in the third dimension with a modest energy cost (quadratic in the mean curvature, with Gaussian curvature taken up in e.g. five or seven-fold rings), thereby producing topologically distinct low-energy structures such as nanotubes [78] and nanocones [79]. However, in very small-diameter nanotubes (below 1 nm in diameter) the curvature penalty of distortion becomes more severe as the bond angles deviate far below the ideal 120 degree sp^2 angles. Here we describe how sp^2 carbon, three-fold coordinated by other carbons, can be replaced by sp^3 carbon, *also three-fold carbon-coordinated*, to produce extremely small-diameter (~ 0.4 nm) highly stable carbon nanowires with minimal bond-angle distortion. Such systems represent the extreme limit of a small-diameter, rigid one-dimensional atomic structure².

The key idea here is to break the tetrahedral symmetry of an sp^3 -hybridized carbon precursor by attaching one relatively tightly-bonded group (e.g. hydrogen or fluorine) and three more weakly bonded groups (or an element like iodine) as shown in Figure 4.7. Eliminating the weakly bonded groups then produces a carbon building block with three reactive bonds per carbon, whose mutual angles match well to a highly curved small-radius cylinder. The precursor molecule could

²Geometrically, one could construct a smaller rigid structure from a triangular atomic motif, but such a bonding geometry, regardless of the type of atom, is not nearly as stable as carbon sp^3 bonds.

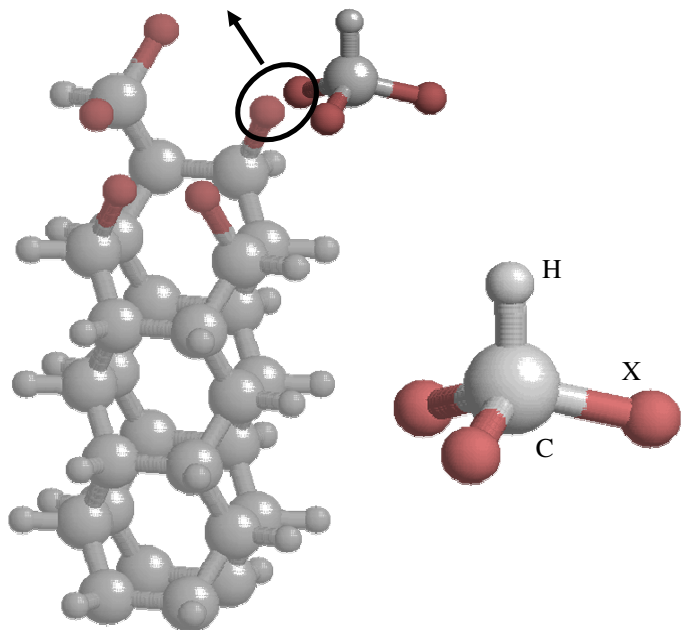


Figure 4.7. The proposed precursor (could be CHI_3) and an illustrative growth configuration showing the role of the capping ligand.

also contain multiple carbons (e.g. $\text{C}_2\text{H}_2\text{X}_2$), so long as each carbon has exactly one relatively inert ligand.

The resulting carbon structures satisfy Euler’s rules for closed polyhedra in exactly the same manner as does carbon in more familiar sp^2 structures, so long as one ignores the topologically irrelevant capping ligand on the fourth bond. Since the stoichiometry of tightly-bound ligands is fixed at one per carbon, it is impossible to form a capped three-dimensional interlinked hexagonal ring structure without rearranging these ligands. (In the small-radius tubes that we consider, energetically unfavorable rings of fewer than five sides are also required to form an Euler cap.) Therefore, if growth conditions are such that the capping ligands are tightly bound and immobile, then the system will always have an active growth edge, whose energy is minimized by restriction to a small-radius one-dimensional growth axis.

The result is an extended one-dimensional structure formed from pure hexagonal rings³. The symmetry analysis developed for the usual nanotubes [80] remains

³Strictly speaking, to guarantee that Euler’s rule is satisfied one must also assume that the endcap atoms are also three-fold coordinated, but this restriction does not affect the allowed

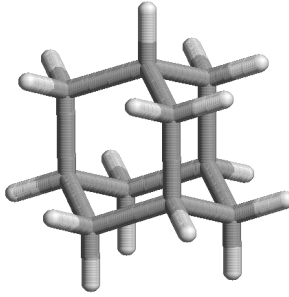


Figure 4.8. Adamantane is an alkane with four fused hexagonal rings.

applicable, except now we have two types of atoms, so the tubes are described by two orbits of the group action. One can even follow an analogous wrapping-index naming convention as for sp^2 carbon nanotubes: the most stable sp^3 tubes, and the ones which we examine in detail, are then the (3,0) and the (2,2) tubes shown in Figure 4.9. The (3,0) tube is essentially a polymer of a close variant of adamantane [81] shown on Figure 4.8, the most stable hydrocarbon known when measured as the binding energy per carbon atom.

We have performed density functional total energy calculations in the norm-conserving pseudopotential approximation for the (2,2) and (3,0) sp^3 -carbon nanotubes. As a basis for the representation of the Kohn-Sham equations we used plane waves with the cutoff energy of 816 eV. To fully exploit the tube symmetry, we arranged the (2,2) nanotubes in a square lattice and the (3,0) nanotubes in a hexagonal lattice. The distance between the axes of the adjacent tubes is held at 10.5 Å so that the interaction between tubes is negligible and we can use a purely axial k-point grid (of eight points). Atoms are described with Troullier-Martins pseudopotentials [12] with cutoff radii of 0.619 Å for carbon and 0.360 Å for hydrogen.

The calculated bond lengths (see Figure 4.9) are similar to C–H and C–C bond lengths in alkanes (i.e. 1.11 Å and 1.54 Å). The bond angles are close to the ideal tetrahedron value, 109.5°, so the material comprises a nearly optimal sp^3 bonding structure with no dangling bonds. Therefore the band structures (Figure 4.10) have large bandgaps typical of saturated hydrocarbons. These bandgaps greatly

bonding geometries in the body of the tube. See [31] for a more complete discussion of local and global topological constraints.

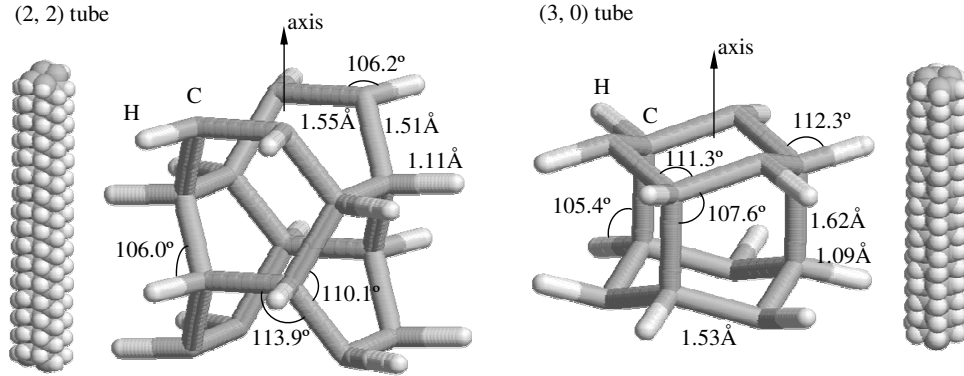


Figure 4.9. The relaxed structures of the (2,2) and (3,0) tubes. The (2,2) tube wire-frame image shows two unit cells. On sides are space-filling models of the tubular structures.

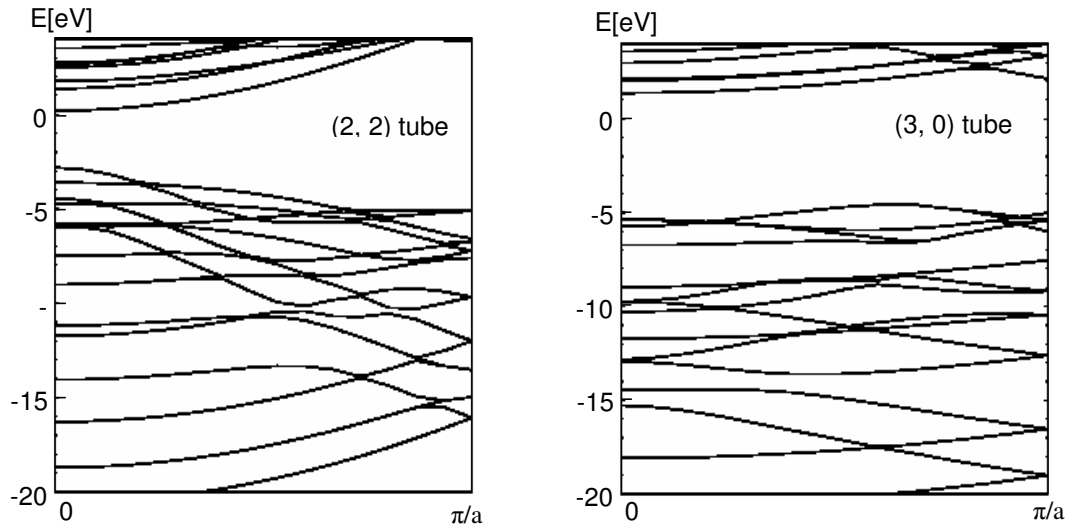


Figure 4.10. The electronic band-structures of the (2,2) and (3,0) nanotubes, showing the large bandgap. Residual band folding is visible. The (3,0) tube has weakly dispersive bands due to the rather long axial carbon-carbon bondlength of 1.62 Å. Horizontal axes use the same scale in both plots.

exceed those obtainable in sp^2 carbon nanotubes, since in that case the semiconducting bandgap arises solely from a nanometer-scale circumferential boundary condition [82], whereas in sp^3 -tubes the gap arises from the local sp^3 bond saturation. The bands of the (3,0) tube are particularly flat, due to relatively long axially directed carbon-carbon bond (1.62 Å). Longer distance between axial atoms means that the interaction along the periodic direction is smaller and thus the energy is

less dependent on the k -vector. The lower bands of the (2,2) nanotube seem to evoke the folded bandstructure of a hydrogenated graphene-like sheet. The large bandgaps and binding energies of these structures (see below) suggest that their synthesis should be favored so long as capping can be maintained on the final sp^3 bond, which should be possible for judicious choice of feedstock molecule (i.e. one with three weak C–X bonds, such as C–I and one strong C–Y bond, such as C–H) and growth conditions (i.e. which differentially favor the breaking of C–X above C–Y).

The *ab initio* total energies for the (2,2) and (3,0) tubes are very close: the (2,2) tube is favored by roughly 0.05 eV per carbon atom. The (2,2) tube is also 0.22 eV per carbon atom *more stable* than benzene, a well-known cyclic hydrocarbon of identical 1:1 carbon:hydrogen stoichiometry. To compare with standard sp^2 -bonded tubular structures, one must create a reference system comprising a purely carbon sp^2 tube of similar diameter plus the requisite number of isolated H_2 molecules. Since sp^2 tubes so small in diameter do not exist, we favor the sp^2 system slightly and compare the sp^3 systems to standard (4,0) and (6,0) tubes plus the appropriate H_2 's. Our proposed (2,2) is 1 eV per carbon atom and 0.55 eV per carbon atom more stable, respectively, than the (4,0) and (6,0) sp^2 variants. (It is also 0.11 eV per carbon atom more stable than the “infinite-radius” limit of a graphene sheet plus molecular hydrogens). Earlier theoretical considerations [83] and simulations [84] suggested that the (4,0) tube is the thinnest possible metastable sp^2 carbon nanotube. Such thin tubes have just recently been synthesized, but only inside of multiwall nanotubes [22, 85] or zeolite channels [86], which surround the tube and stabilize its delicate structure.

The (2,2) and (3,0) sp^3 tubes extend one-dimensional carbon systems to the smallest possible radii. They are also the beginning of an entire family of sp^3 tubes. As the tube diameter increases, it becomes untenable to populate only the outer surface with capping hydrogens, since bond angle distortions become severe. However, by inverting some capping ligands onto the *inner* surface, one can stabilize these larger structures. Figure 4.11 depicts the stablest geometries (calculated within a tight binding total energy formalism [4]) for the (8,8) and (5,0) sp^3 tubes. Unrolled, the (8,8) system forms a pleated honeycomb C–H plane with up-down alternated hydrogens, similar to the pleated structure considered for

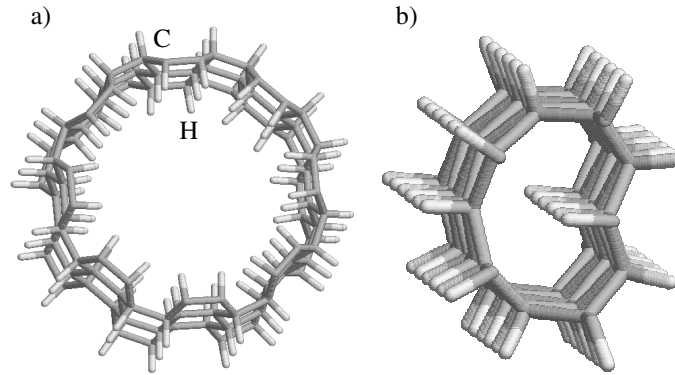


Figure 4.11. The tight-binding relaxed structure of (a) the (8,8) and (b) the (5,0) sp^3 tube (three unit cells are showed).

some Si-H systems [87]. The tubes undergo an interesting transition from purely external capping groups to a mixture of internal and external caps as the radius increases. For example, within tight binding the (4,0) structure is most stable with entirely external hydrogen. In contrast, the preferred (5,0) structure has one row of hydrogen on the inner surface. These inner hydrogens minimize bond angle distortions by increasing the mean curvature of the remaining surface. Within the tight binding total energy scheme, the total energies per carbon atom for all of the sp^3 tubes studied are only slightly higher than that of the (2,2) tube (by 0.1 to 0.15 eV) and remain more stable than benzene [88].

It is particularly fascinating to consider the results of partially removing hydrogen (e.g. thermally) from an sp^3 tube to form a mixed sp^2/sp^3 hybrid with novel electronic boundary conditions and the possibility for tuning semiconducting/metallic properties similar to that described for graphene strips [89] (see also the next section). Such partial removal may be particularly facile for the tubes in the transition region of diameter between pure external and mixed internal/external capping ligands.

The smallest-diameter (2,2) and (3,0) sp^3 tubes are also extremely stiff. A calculation of Young's modulus requires as input a meaningful cross-sectional area perpendicular to the axis of the tube. One must take particular care in defining this area for very thin tubes. We define the cross-sectional area of the (2,2) and (3,0) tubes as that corresponding to an equivalent number of carbon atoms in a core sample through a bulk diamond structure. The reference to a bulk structure of sim-

ilar bonding geometry minimizes the arbitrariness in defining the “outer surface” of the tube. Bulk diamond (when calculated here with the same pseudopotential method) has a volume of 5.536 \AA^3 per carbon atom. Assigning a similar volume per atom to the tubular structures⁴, the appropriate volumes of the (2,2) and (3,0) unit cells are 17.94 \AA^3 and 15.94 \AA^3 respectively. Dividing by the (well-defined) unit cell lengths, the resulting cross-sectional areas are equivalent to those of disks with radii of 2.39 \AA and 2.25 \AA respectively. Such values are quite reasonable, considering the transverse dimensions of the structures given in Figure 4.9. The corresponding Young’s moduli are 1.78 TPa for the (3,0) tube and 1.53 TPa for the (2,2) tube. These values are substantially larger than those of more familiar sp^2 nanotubes: the (4,0) tube, calculated here with a similar method, has a Young’s modulus of 1.18 TPa. Earlier calculations [90] for single sp^2 tubes gave 1 TPa, while experimental results [91] cluster around 1.3 TPa.

Since cross-sectional areas are really only well-defined in macroscopic systems, a more direct and fair comparison between sp^2 and sp^3 carbon tubes is provided by the following thought experiment: Given a box of N carbon atoms and a distance L to span with filament(s) of maximal stiffness, should one choose sp^2 or sp^3 structures? The suitable quantity of comparison is then the stiffness per unit linear carbon atom density along the axis. This quantity (in units 10^{-8} Jm^{-1}) is 3.44 for the (2,2) tube, 2.36 for the (3,0) tube and only 1.59 for a (4,0) sp^2 tube (larger-diameter sp^2 nanotubes have only slightly larger values). From both points of view, these new sp^3 structures are more rigid than traditional sp^2 tubes, which were previously believed to be the most rigid structures known.

Carbon nanotubes ultimately depend for their stability on the topological rules which allow three-fold coordinated atoms to form extended open polyhedra (or equivalently, closed polyhedra of genus one [31]) of arbitrary length in systems with exclusively hexagonal faces. We demonstrate here that sp^3 bonded carbon can assume the same topology as sp^2 , so long as the fourth bond is capped with a tightly-bound ligand. The resulting structures possess unique properties inaccessible in their sp^2 cousins: a very large insulating bandgap, high stability at an extremely small diameter, and Young’s moduli exceeding 1.5 TPa.

⁴The average bond lengths in (2,2) and (3,0) tubes differ only slightly from that in diamond, so this identification is reasonable, particularly for the (2,2) tube.

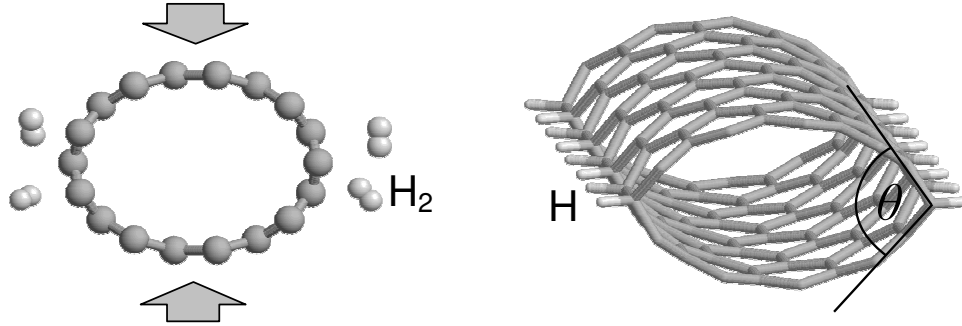


Figure 4.12. Left: Uniaxial compression of a nanotube transverse to its axis in the presence of hydrogen molecules could facilitate chemisorption onto diametrically opposed rows by forcing these carbon atoms into an sp^3 configuration, as shown on right. The aperture angle θ of the sp^3 junction is used later in the discussion of structural energetics.

4.4 Eye Tubes

In the past several years, the research focus for carbon nanotubes has turned from the properties of the nanotubes alone towards their modification— for example, by doping, deformation or incorporation into nanodevices [92]. In particular, chemical and physical adsorption onto the nanotube surface provides a powerful way to tune electronic properties. Chemisorption converts sp^2 carbon into sp^3 carbon, without destroying the original hexagonal network. This process has been performed with both hydrogen [93] and fluorine [70]. Previous theoretical studies of hydrogenated single wall nanotubes at complete or 50% hydrogen coverage [66] generally show a band gap that increases with coverage, except for some special half-coverage patterns when the tube becomes a band-crossing metal. Unfortunately, it is unclear experimentally how to create uniform (i.e. translationally invariant) patterns of chemisorption. Graphene nanoribbons [89, 96] show novel edge states with very low dispersion. These ribbons have been synthesized [97], but the possibility of controlling their geometry (especially endings) seems remote [98]. Here we propose a plausible means to synthesize pairs of weakly coupled high-quality graphene ribbons by selective chemisorption onto carbon nanotubes. Pressing a nanotube transverse to its axis forces two diametrically opposed rows of carbon atoms into high curvature sp^3 -like configurations, rendering them specially favorable chemisorption sites (see Figure 4.12). The p_z orbitals of the atoms which bond

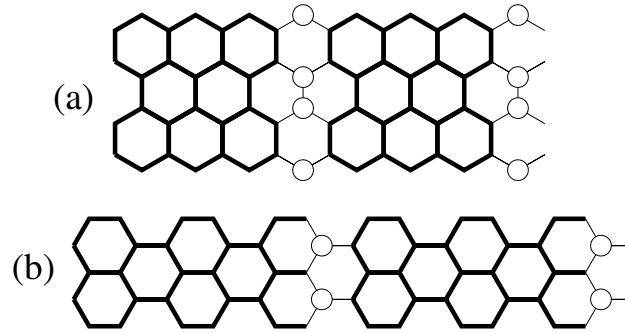


Figure 4.13. (courtesy of Paul Lammert) Chemisorption patterns on (a) zig-zag and (b) armchair nanotubes. Open circles indicate adsorption sites and the absence of an accessible p_z orbital. Heavy bonds symbolize electronic π -hopping in the tight-binding picture; the light bonds are inactive.

to hydrogen become unavailable to the π -complex; this separates the nanotube into a pair of ribbons. This violent rearrangement of the π manifold has surprisingly little effect on the electronic states of $(n,0)$ tubes and actually *decreases*, rather than increases, the bandgap. An electronically bifurcated (n,n) tube has pairs of exceptionally flat and closely spaced bands at the Fermi level. As we will see, energies of electronic states near the Fermi level are so close that the ground state stabilizes in a *magnetic* state with two top valence bands half filled with the same spin electrons.

The transformation from sp^2 to sp^3 hybridization gives the tube an eye-like cross-section, as shown in Figure 4.12. We have performed a series of ab-initio calculations using the projector augmented wave (PAW) method within generalized gradient approximation (GGA) of density functional theory (DFT), as implemented in the VASP package [74], plus selected tight binding calculations to reveal essential physics. Relaxation was performed using at least 5 k-points along the axis in the self-consistent loop⁵.

Straight columns of chemisorbed hydrogen can be realized only on zig-zag and armchair tube walls, so we focus on these two types of tubes. Figures 4.14 and 4.15 summarize electronic properties of metallic eye tubes. For $(3n,0)$ tubes, the original bands (which nearly touch E_F at the Γ point) split, producing overlap-

⁵The plane waves basis energy cutoff was 400 eV. The relaxation energy convergence criterion for electronic loop was $1.0 \cdot 10^{-4}$ and for ionic loop it was set to be $1.0 \cdot 10^{-3}$.

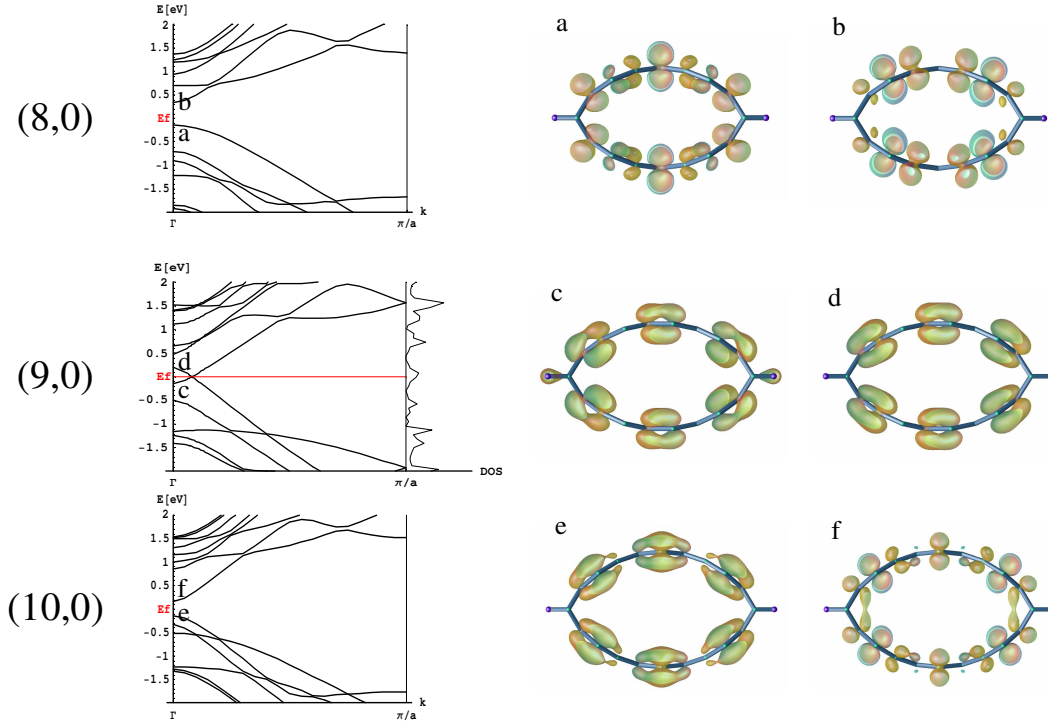


Figure 4.14. PAW GGA band plots with density of states and the electron probability density plots (density isosurfaces for 0.003 \AA^{-3} are shown) for the highest occupied and lowest unoccupied states at Γ for (8,0), (9,0) and (10,0) eye tubes. In each case, the wavefunction has a node on the sp^3 carbon.

ping bands in the eye. The $(3d - 1, 0)$ and $(3d + 1, 0)$ zig-zag eye tubes remain semiconducting with somewhat smaller band gaps compared to the parent clean tubes. For example, the (8,0) tube gap decreased from 0.59 eV to 0.48 eV, while the (10,0) tube gap went down from 1.04 eV to 0.29 eV after hydrogenization. The armchair tubes show dramatic changes, with entirely new bands appearing near the Fermi energy.

Using a generalization of the ribbon theory [89, 96], Paul Lammert reached a deeper understanding of most of the electronic features of eye tubes. Conceptually, we can produce an eye tube in two steps. First, chemisorption removes the p orbitals of hydrogenated carbon atoms from the π -complex near the Fermi energy. Those atoms therefore become inert as far as the low-energy electronic structure is concerned, and the tube is severed into two ribbons separated by a pair of thin stripes (i.e. the hydrogenated atoms), see Figure 4.13(a). Second, the ribbons are coupled electronically by orbital overlap. This coupling is strengthened by the

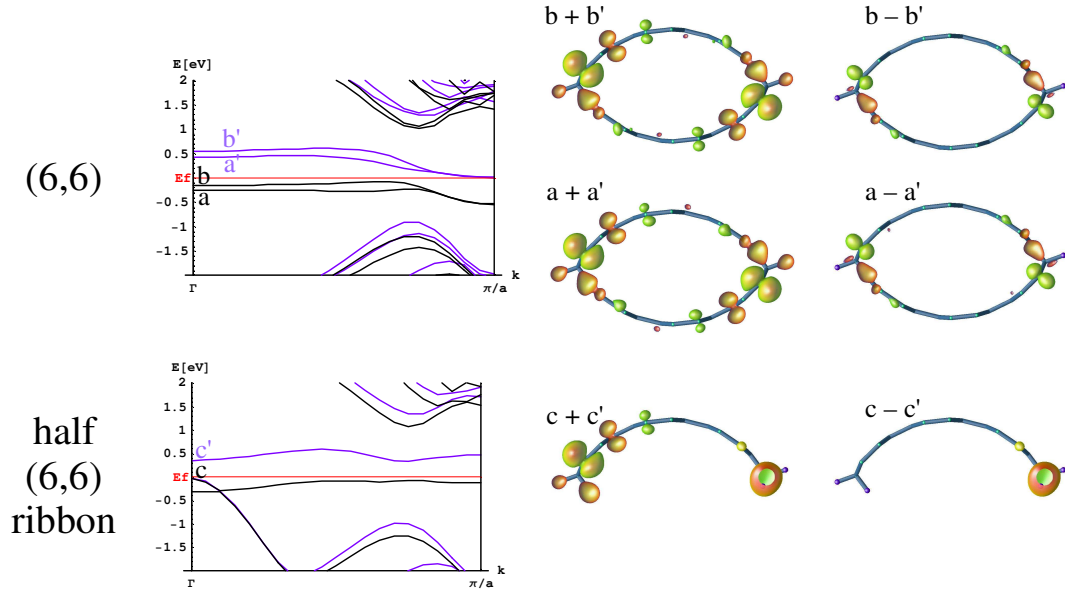


Figure 4.15. Left: PAW GGA spin polarized band structures showing uneven spin population on the Fermi level (blue and black curves represent two spin polarizations) for (6,6) eye tube and its half, a bended (unrelaxed) graphitic ribbon terminated with hydrogens at positions where carbon atoms are in the eye tube. The electron probability density plots for combined spin and spin difference shown on the right (density isosurfaces for 0.003 \AA^{-3} are shown) for the highest occupied and lowest unoccupied states at the gamma point illustrate electronic bifurcation in the eye tube and close connection to the ribbon's edge state. In both cases carbon-carbon bonds in the circumferential direction lengthen gradually from 1.40 \AA at the zig-zag edge to 1.58 \AA at the bearded edge, nearly the same as the change from a double bond to single bond.

flattening of the ribbons which occurs under structural relaxation.

For the zig-zag case, the electronic bands in a single ribbon have a simple relationship to those of the parent clean $(n, 0)$ nanotube. The bands in the nanotube are labelled by angular pseudomomentum m , with m and $-m$ degenerate. In a tight-binding view, one linear combination of m and $-m$ has zero amplitude on the stripes, and these states form the eigenstates of the ribbon. Conversely, if the upper uncoupled ribbon carries a particular eigenstate and the lower ribbon carries its reflection and the amplitude on the stripes is set to zero, the result is an energy eigenstate of the parent tube. The phase relationship between the wavefunctions on the two ribbons ensures that the hopping Hamiltonian maintains zero amplitude on the stripes. Therefore, the uncoupled ribbons should have

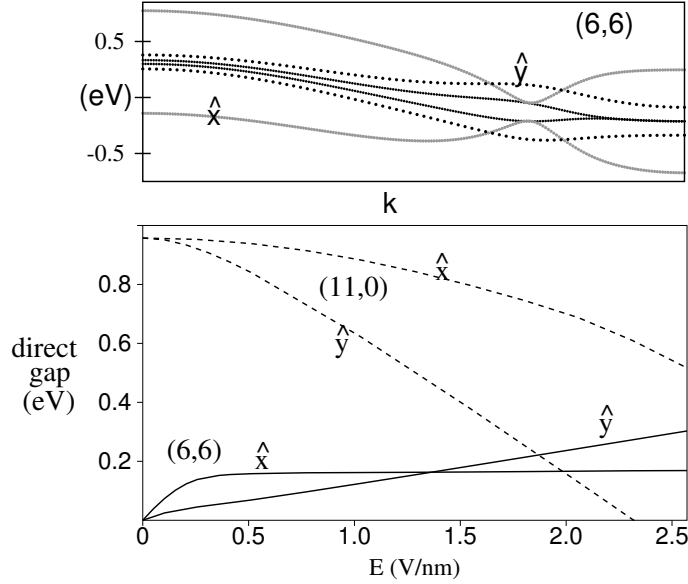


Figure 4.16. (courtesy of Paul Lammert) Upper panel: tight-binding results for the near-Fermi-energy bands of the (6,6) eye tube. The solid line is in zero field, the gray line for $\mathbf{E} = 1$ V/nm \hat{x} , and the dashed line for $\mathbf{E} = 1$ V/nm \hat{y} . The individual band widths are significantly larger than found in GGA; the band separation is in much better agreement. Lower panel: minimum direct gap between the bands as a function of field. The solid lines are for the (6,6) eyetube and the dashed lines for the (11,0) eyetube. The direction of the field is indicated by x or y . Since the tight-binding calculations are not self consistent, the values of electric field should be interpreted in terms of voltage drop across the eye.

band structures very similar to that of the parent tube, but lacking the double degeneracies (and excepting one or two of the parent tube bands which lack partners under $m \mapsto -m$).

In the second step, the weak coupling between ribbons splits the bands into bonding and antibonding combinations. The most striking manifestation of this splitting is the shift of the Fermi level band crossing away from the Γ point in the $(3n, 0)$ tubes (as an example, (9, 0) eye tube band plot is given on Figure 4.14). The bands which cross there are doubly degenerate. For $(n, 0)$ eye tubes derived from semiconducting tubes, the band structures are very similar to those of the parent tubes, except for the splitting which results in more bands, and consequently a small decrease of the gap.

Armchair eye tubes are entirely different, as shown in Figure 4.15. The band

structure near the Fermi energy bears little resemblance to that of the parent nanotube, with a pair of very narrow bands. Again, we appeal to the ribbon theory for an explanation in Paul Lammert's formulation. The ribbon-stripe structure for these tubes, shown in Figure 4.13(b), has a zig-zag edge on the left, and a *bearded edge* [99] on the other side, which is in the same sublattice as the atoms of the zig-zag edge. As shown in refs. [89, 96], with a zig-zag ribbon edge oriented along the z-axis, there are zero-energy states localized to the edge for $k_z a > 2\pi/3$ ($a = 1.42 \text{ \AA} \cdot \sqrt{3}$ is the graphene lattice constant); these decay with distance x from the edge as $[2 \cos(k_z a/2)]^{x/a}$. If the ribbon has finite width and the opposite edge is also zig-zag (hence on the other sublattice), then the opposite edge is only a small perturbation. The members of the same family of functions with $k_z a < 2\pi/3$ are not approximate eigenstates since they grow with distance from the edge ($2 \cos(k_z a/2) > 1$), so that the opposite edge is not a small perturbation. However, if the opposite edge is bearded, its presence requires no modification of the wavefunction, because it is on the same sublattice. Thus, this ribbon has an edge state very near E_F for all k_z . If $k_z a > 2\pi/3$, it is localized near the zig-zag edge, and if $k_z a < 2\pi/3$, it is near the bearded edge. Near $k_z a \approx 2\pi/3$ the wavefunction is well-distributed over the ribbon, and so loses its edge character. When two such zig-zag/bearded ribbons are combined into an eye tube, the two degenerate flat bands contributed by the ribbons develop a bonding/anti-bonding splitting. The ab initio results in Figures 4.15 are in harmony with these simple tight-binding predictions. The lower part of Fig 4.15 shows results for a ribbon plus stripes frozen in the conformation of the relaxed eye tube. (Dangling bonds are simply capped with hydrogen.) The charge density of the state in the flat band at Γ , shown at lower inset on right, is concentrated on the bearded edge of the ribbon.

Band structures on Figure 4.15 also show an unequal spin population in the armchair tube. This is an unexpected behavior for a carbon-based system with an even number of electrons. We have confirmed that there is no Peierl's dimerization in the system by repeating our calculation for the double unit cell eye tube. This result shows that the armchair eye tubes have macroscopic magnetic ordering. The uneven spin population in eye tubes is currently a subject of an ongoing research

inside our group⁶. This effect can be again connected to the ribbon edge state. In ref. [99] a Hubbard model for the flat band wavefunction is constructed, which shows that the magnetic ordering in a zig-zag ribbon is a consequence of one bearded edge.

The pair of flat bands near the Fermi energy in armchair eye tubes, half filled in the undoped tube, could produce unusual and potentially useful optical properties. An accurate optical transition analysis for these systems requires use of the two-particle Greens function for electron-hole excitations [100], a method beyond the GW approximation. It has been shown that this advanced approach is already essential for an accurate optical spectra calculation in clean tubes [101] and in eye tubes it is even more important, due to narrowness of the flat bands on the Fermi level. For now, we have been able to make only a very limited DFT calculation of the joint density of states, which shows that the eye tubes could have exceptionally big response in the terahertz range. This is interesting for possible applications, since tubes are much lighter materials than the common narrow-band materials as PbTe and SnTe and the absorption peak may be highly tunable by means of mechanical stress.

The relative weakness of the coupling between the ribbons comprising an eye tube also makes the band structure highly susceptible to applied static electric fields, compared to a clean nanotube. Figure 4.16 summarizes the effects of an external field, according to Paul Lammert's tight-binding [108] calculations (without spin) applied to the relaxed eye tube structures. The lower panel of Figure 4.16 shows the evolution of the minimal direct gap for the (6,6) and (11,0) eye tubes with field along either the x or y direction (x is the long direction across the eye). Compared with a clean tube [104], the gap of the (11,0) eye tube is closed by a very modest field along y , because it is necessary only to overcome the weak coupling between the two ribbons in order to completely polarize the bands. The polarizability along x is not as large, since the field is now principally along the ribbons.

In the armchair eye tubes, the twin bands near the Fermi energy consist of edge states, so that a larger response is expected for a field along x . As measured by the minimal direct gap, however, this is true only for small fields. The minimal direct

⁶Our gratitude is due to Prof. Peter Eklund for pointing out the possibility of this effect.

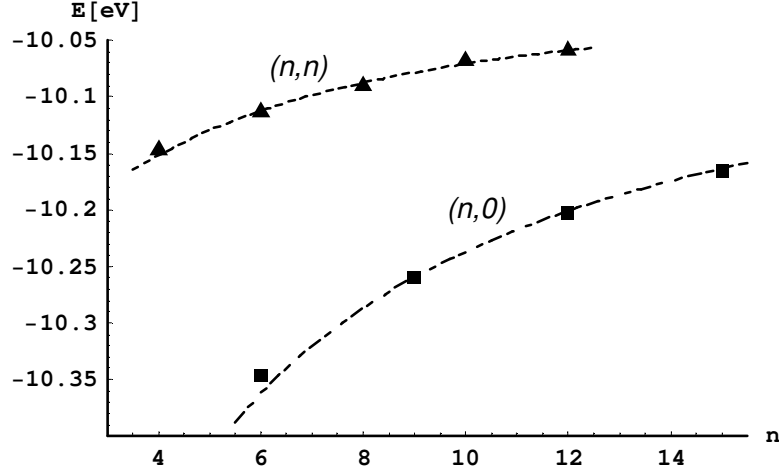


Figure 4.17. The energy per carbon atom from DFT calculations and the fit of Eq. (4.2) with coefficients given in text for (n, n) and for $(n, 0)$ eye tubes.

gap saturates for a field along x , whereas it continues to rise roughly linearly for the field along y . A closer look at the effect of the field on the bands, as shown in the upper panel of Figure 4.16, reveals the source of the saturation. The k -point at which the edge states switch from one edge to the other is special. At that k , there is complete insensitivity to an electric field along \hat{x} , and that point in the band determines the gap for large enough fields. Since there is no k at which the upper and lower ribbon states have zero y -component of dipole moment, there is no such saturation for a field along \hat{y} .

The structural energetics of eye tubes can also be decomposed into contributions from sp^2 -like and sp^3 -like regions:

$$E_{eye}(n) = N_{sp3} \varepsilon_{sp3} + N_{sp2} \left[\varepsilon_g + y_{eff} \left(\frac{1}{R_{eff}} \right)^2 \right]. \quad (4.2)$$

The first term is the energy of sp^3 atoms. Each unit cell has $N_{sp3} = 2$ sp^3 atoms in case of (n, n) and $N_{sp3} = 4$ for $(n, 0)$ tubes. The fitted sp^3 energy per one sp^3 carbon is $\varepsilon_{sp3} = -12.04$ eV for (n, n) and $\varepsilon_{sp3} = -12.95$ eV for $(n, 0)$ tubes. The difference comes from a different edge sp^2 - sp^3 bond frustration produced by different orientations of hexagons on the tube walls. The second term in Eq. (4.2) comes from the sp^2 part of the tube, expressed in terms of the number of sp^2 atoms

per unit cell $N_{sp2} = 4n - N_{sp3}$, an effective radius of curvature R_{eff} and effective bending modulus y_{eff} . R_{eff} is larger than the radius $R(n)$ of the parent clean tube, since the rows of sp^3 atoms absorb some of the curvature. It is defined as $R_{eff}(n) = \pi R(n)/\theta(n)$, with $R(n) = a_o n \sqrt{3}/(2\pi)$ for $(n, 0)$ and $R(n) = 3 a_o n/(2\pi)$ for (n, n) tubes. The aperture angle $\theta(n)$ of the sp^3 joint (see Figure 4.12) is only weakly dependent on n and can be fit by a line over the range of sizes studied: $\theta(n) = 1.77 + 0.05n$ for (n, n) tubes with $4 \leq n \leq 12$ and $\theta(n) = 1.90 + 0.01n$ for $(n, 0)$ tubes with $6 \leq n \leq 15$. From calculation on clean tubes we find $\varepsilon_g = -9.99$ eV (the graphene energy per atom)⁷ and $y_{eff} = 2.035$ Å²eV (the effective elasticity of graphene sheet). As Figure 4.17 shows, the energy difference between DFT energy and the fit (4.2) is smaller than 3 meV per carbon atom, except for small eye tubes, for which the continuum elastic approximation is least suited⁸.

We have presented a systematic study of zig-zag and armchair carbon nanotubes with two diametrically opposed stripes of chemisorbed hydrogen. A qualitative understanding of many of the salient electronic features is provided on the basis of the graphene-ribbon theory. Metallicity of $(3n, 0)$ tubes is maintained despite a substantial structural change after the hydrogen chemisorption. In armchair eye tubes, a spin polarized population of a pair of very narrow bands near the Fermi energy (despite an even total number of electrons), raises many interesting fundamental and application-related questions, which should be addressed in the future of this project.

⁷A separate graphene sheet DFT relaxation with the same parameters, 18x18x1 k-points mesh and 10 Å between graphene layers gives $\varepsilon_g = -10.13$ eV per carbon atom.

⁸For the (4, 4) tube the difference is 5 meV and for the (6, 0) tube it is 16 meV per carbon atom.

Chapter 5

Conclusion

This text documents our investigation of carbon systems and their interaction with hydrogen. It is an illustration of a fruitful connection between applied and fundamental science. Our work was originally motivated by a practical problem of hydrogen storage and then gradually shifted toward evaluation of the nature of hydrogen adsorption in carbon materials, which then resulted in a design of new materials with very interesting and potentially useful, mechanical and electronic properties.

We first discussed the pure-carbon systems and among them the nanoporous carbon schwarzite model, where we showed how hexagonal arrangement of sp^2 carbon atoms produces especially stable electronic state of a graphenic sheet. Each non-hexagonal ring in such system introduces frustration in electronic subsystem around atoms not able to properly pair all of their electrons.

Next, we discussed the hydrogen adsorption on carbon surfaces in its two limiting cases. In the weak limit, hydrogen physisorbs on the carbon surface in a molecular form, confined in a shallow potential well of 0.05 to 0.1 eV at a distance of about 2.6 Å from the carbon surface. In this case hydrogen molecules interact with carbon atoms through a weak dipole-dipole (Van der Waals) correlation. This interaction is particularly difficult for accurate first principles modeling. We collaborated with Jeffrey Grossman to make a precise Diffusion Monte Carlo calculations on a representative patch of preprocessed nanotube surface. These calculations showed that the local distortions of the sp^2 carbon bonds are crucial for the strength of hydrogen physisorption. We demonstrated how these distor-

tions can be produced by irregularities (pentagonal and heptagonal rings) in the carbon hexagonal network or as a consequence of the surface curvature.

In the strong adsorption limit, hydrogen molecules dissociate (usually with help of some catalyst) to atoms, which then make chemical bonds with the carbon host atoms on the graphitic surface. In this case the atomic hydrogen is held in a potential well of 0.5 to 1 eV (relative to the hydrogen molecule) and about 1.1 Å away from carbon surface. Upon chemisorption the underlying carbon hexagonal network still retains its topology, but becomes distorted due to a change in the electronic system. A chemisorbed hydrogen atom forces the carbon host to change its electronic configuration toward sp^3 hybridization, producing a tetrahedron-like puckering on the carbon surface, which affects the neighboring carbon atoms, distorting their bonds. As a result, chemisorption of the first few hydrogens is not energetically favorable. However, as we have shown, if hydrogen is allowed to access both sides of the carbon surface, then the same puckering effect stabilizes a cluster of chemisorbed hydrogens after some critical size of about 5-10 atoms (depending on the surface curvature) and the further chemisorption proceeds as an exothermic process. We explained this behavior by considering reinforcement of chemisorbed hydrogens through an orchestrated deformation of the underlying carbon network. This in turn brought to our attention the potential of chemisorption to change properties of carbon nanotubes, an idea we have developed in the next two projects.

In one project, we considered sp^3 carbon-hydrogen tubes, which can be obtained starting from a usual tube and replacing every carbon atom with a carbon-hydrogen pair. In experiments, these tubes could be synthesized starting from a CHX_3 precursor, where X is some weakly bonded group or maybe an element like iodine. Eliminating the weakly bonded groups then produces a carbon building block with three bonds per carbon atom, as it should be in a tube. Since in the resulting structures, carbon atoms use all their electrons for sigma bonding, all sp^3 tubes are insulators. Our calculations showed that there is a very stable family of sp^3 tubular structures all the way down to the smallest possible tube radii. Moreover, we predicted that the smallest diameter sp^3 tubes are among the stiffest one-dimensional systems known. Since the cross-sectional surface area is not well defined for such tiny objects, we calculated spring constant per linear atomic density as a measure of stiffness. In this sense, sp^3 tubes are about 40 percent stiffer

than usual tubes.

In our another project, carbon atoms are partially replaced with carbon-hydrogen pairs along two diametrically opposite sides of the tube. Since these pairs have carbon atoms without p_z orbitals, they electronically separate tube into two sp^2 ribbons connected with columns of sp^3 atoms. We propose an experiment to make these tubes through a controlled hydrogen chemisorption where a tube is compressed transverse to the axis in presence of hydrogen. A tube compressed in such a way has an increased curvature of two diametrically opposite wall regions favoring them for chemisorption. Our total energy and electronic calculations confirmed that these tubes can be understood as two weakly coupled graphitic ribbons. Armchair tubes, when so divided, acquire a pair of extremely narrow half-filled bands at the Fermi energy, with corresponding states related to the edge states in zig-zag ribbons. Although this system has an even number of electrons, energies of electronic states near the Fermi level are so close that the ground state stabilizes with two top valence bands half filled with the same spin electrons, similarly to the Hund's rule for atomic energy levels. If the system is doped with electrons or holes, or spin flip is allowed, these tubes could be very active terahertz materials. A logical next step in this project would be a precise optical spectra calculation. This kind of calculations, however, requires so advanced methods and big computer resources that it represents a real challenge at this moment. Looking back, the same kind of challenge on 1999, when this thesis started, is a matter of a routine calculation today. This gives us confidence that in the next several years the eye tubes project will have its natural continuation in theory and quite possible also in experiment.

The field of carbon-based nanostructures is evolving rapidly with new advances in experiment and theory, opening unforeseen possibilities. While the science of nanotubes and related structures has been already quite developed, with thousand of articles published yearly, technology has yet to follow. One of the main obstacles for faster exploitation of nanotubes in industry is our poor ability to structurally control matter on the atomic level. Although today nanotechnology is still the almost exclusive preserve of the state of the art research laboratories, its way toward future applications can be clearly seen illuminated by predictions based on computer simulations. As methods of numerical experiment become more accurate

following advances in algorithms and computer hardware, we can more precisely and confidently investigate materials which have yet to come. However, for more precise predictions it is crucial to have programmers able to make better simulations and physicists able to make better programs. From that point of view, the High Performance Computing Graduate Minor is a step in the right direction as an educational bridge between the scientific and technical communities.

Translational Symmetry

Each basis $\beta = \{a_i | i = 1, \dots, N\}$ in N -dimensional space defines a Bravais lattice $\{\sum_{l=1}^N M_l \vec{a}_l | M_l \in \mathbb{Z}\}$ (\mathbb{Z} is set of all integer numbers) as a set of all points in space which map to each other by translations $\mathbb{T} = \{t_{\vec{a}} | \vec{a} = \sum_l^N n_l \vec{a}_l, n_l \in \mathbb{Z}\}$. These translations are therefore symmetries of the Bravais lattice and they form an Abelian group \mathbb{T} with countably infinitely many elements. As a commutative group, \mathbb{T} has only one dimensional irreducible representations. They are given by $\Delta_{\vec{k}}(t_{\vec{a}}) = \exp(-i\vec{k} \cdot \vec{a})$, where \vec{k} is set of three irreducible indexes.

All operators $T_{\vec{a}} : f(\vec{x}) \mapsto f(\vec{x} - \vec{a})$ in the space of functions $f : \mathbb{R}^3 \rightarrow \mathbb{R}^3$, with \vec{a} being a vector of the Bravais lattice, form a representation $D(\mathbb{T})$ of the translational group \mathbb{T} . For every \vec{k} the set $\{f_{\vec{k}, \vec{G}}(\vec{r}) = \exp(i(\vec{k} + \vec{G}) \cdot \vec{r}) | (\forall l) \vec{G} \cdot \vec{a}_l \in 2\pi\mathbb{Z}\}$ spans a subspace $V_{\vec{k}}$ of functions where $D(\mathbb{T})$ behaves as irreducible representation $\Delta_{\vec{k}}$, since $T_{\vec{a}} f_{\vec{k}, \vec{G}}(\vec{r}) = \exp(-i\vec{k} \cdot \vec{a}) f_{\vec{k}, \vec{G}}(\vec{r})$ (because $\exp(i\vec{G} \cdot \vec{a}) = \exp(2\pi n) = 1$). From the requirement $\vec{G} \cdot \vec{a}_l = 2\pi n$, where n is an integer follows that all vectors \vec{G} form a lattice (called inverse or reciprocal lattice), which consists of integer linear combinations of the inverse basis $\{\vec{b}_l\}$, defined with the system of equations $\vec{b}_k \cdot \vec{a}_l = 2\pi\delta_{kl}$. All unique irreducible indexes \vec{k} fill one primitive cell of this lattice in reciprocal space. The Wigner-Seitz cell of that lattice is called the Brillouin zone. It is especially suitable for manipulations, since it has full point group symmetry of the crystal and its boundaries are the bisecting planes where Bragg scattering occurs.

If the system is symmetric with respect to translation $t_{\vec{a}}$, then any measurement must give the same result before and after translation, which is formally expressed as a demand that the corresponding hamiltonian H must satisfy $H \circ T_{\vec{a}} = T_{\vec{a}} \circ H$, i.e. it must commute with the representation of the translation. If H commutes with all elements of the representation of group \mathbb{T} (the system is \mathbb{T} -translationally

symmetric), then each eigenstate ϕ (eigenvector of H) must be inside one subspace $V_{\vec{k}}$ of the group \mathbb{T} , i.e. for each eigenstate ϕ there is a set of numbers $c_{\vec{k},\vec{G}}$ such that for some \vec{k} :

$$\phi(\vec{r}) = \sum_{\vec{G}} c_{\vec{k},\vec{G}} f_{\vec{k},\vec{G}}(\vec{r}). \quad (1)$$

Then \vec{k} is a good quantum number (preserved in evolution) and it can be used to count the eigenstates of the system. Since the system has atoms in the unit cell, each subspace $V_{\vec{k}}$ is nontrivial (it is actually infinite dimensional) and one more index n should be introduced to distinguish all eigenstates:

$$\begin{aligned} \phi_{n,\vec{k}}(\vec{r}) &= \sum_{\vec{G}} c_{n\vec{k},\vec{G}} f_{\vec{k},\vec{G}}(\vec{r}) = \\ &= \sum_{\vec{G}} c_{n\vec{k},\vec{G}} \exp(i(\vec{k} + \vec{G}) \cdot \vec{r}) = \exp(i\vec{k} \cdot \vec{r}) \sum_{\vec{G}} c_{n\vec{k},\vec{G}} \exp(i\vec{G} \cdot \vec{r}) = \\ &= \exp(i\vec{k} \cdot \vec{r}) u_{n\vec{k}}(\vec{r}). \end{aligned} \quad (2)$$

The function $u_{n\vec{k}}(\vec{r}) = \sum_{\vec{G}} c_{n\vec{k},\vec{G}} \exp(i\vec{G} \cdot \vec{r})$ is a symmetric (translationally periodic) function of the group \mathbb{T} . This is an expression of the Bloch theorem, which states that for a translationally periodic system, any eigenstate is a product of $\exp(i\vec{k} \cdot \vec{r})$ and a periodic function $u_{n\vec{k}}(\vec{r})$.

Bibliography

- [1] N. Ashcroft and N. Mermin, *Solid State Physics*, Holt, Rinehart and Winston (1976).
- [2] H. J. Monkhorst and J. D. Pack, Phys. Rev. B **13**, 5188 (1976).
- [3] R. Martin, *Electronic Structure*, Cambridge University Press (2004).
- [4] D. Porezag, Th. Frauenheim, Th. Kohler, G. Seifert, and R. Kaschner, Phys. Rev. B **51**, 12947 (1995).
A. P. Horsfield, Phys. Rev. B **56**, 6594 (1997).
- [5] J. C. Slater and G. F. Koster, Phys Rev. **94**, 1498 (1954).
- [6] W. Kohn, Rev. Mod. Phys. **71**, 1253 (1999).
- [7] P. Hohenberg and W. Kohn, Phys. Rev **136**, B864 (1964).
- [8] W. Kohn and L. J. Sham, Phys. Rev. **140**, A1133 (1965).
- [9] M. Levy, Phys. Rev. A **26**, 1200 (1982).
- [10] D. M. Ceperley, Phys. Rev. B **18**, 3126 (1978);
D. M. Ceperley and B. J. Alder, Phys. Rev. Lett. **45**, 566 (1980).
- [11] K. Burke and friends, *The ABC of DFT*, <http://dft.rutgers.edu/kieron/beta>
- [12] N. Troullier, J. L. Martins, Phys. Rev. B **43**, 1993 and 8861 (1991).
- [13] L. Kleinman and D. M. Bylander, Phys. Rev. Lett. **48**, 1425 (1982).
- [14] D. Vanderbilt, Phys. Rev. B **41**, 7892 (1990).
- [15] P. E. Blöchl, Phys. Rev. B **41**, 5414 (1990).
- [16] P. E. Blöchl, Phys. Rev. B **50**, 17953 (1994).
- [17] *CRC Handbook of Chemistry and Physics*, 65th Edition, CRC Press, Inc., Boca Raton (1985).

- [18] S. E. Haggerty, *Science* **285**, 851 (1999).
- [19] T. S. Metcalfe, M. H. Montgomery and A. Kanaan, *Astrophys. J.* **605**, L133 (2004)
- [20] L. A. Hemstreet, Jr., C. Y. Feng, M. L. Cohen, *Phys. Rev. B* **2**, 2054 (1970).
- [21] M. S. Dresselhaus, G. Dresselhaus, P. C. Eklund, *Science of Fullerenes and Carbon Nanotubes : Their Properties and Applications*, Academic Press (1996).
- [22] L.-C. Qin, X. Zhao, K. Hirahara, Y. Miyamoto, Y. Ando and S. Iijima, *Nature* **408**, 50 (2000).
- [23] M. Ouyang, Jin-Lin Huang, and C. M. Lieber, *Acc. Chem. Res.* **35**, 1018 (2002).
- [24] R.K. Mariwala and H.C. Foley, *Ind. Eng. Chem. Res.* **33**, 2314 (1994).
- [25] Y. Gogotsi, A. Nikitin, H. Ye, W. Zhou, J. E. Fischer, B. Yi, H. C. Foley and M. W. Barsoum, *Nature Materials* **2**, 591 (2003).
- [26] E. A. Lord and A. L. Mackay, *Curr. Sci.* **85** 346 (2003).
- [27] S. Andersson, T. S. T. Hyde, F. Kare Larsson and S. Lidint, *Chem. Rev.* **88**, 221 (1988).
- [28] H. Schwarz, *Monatsber. Berlin Akad.*, Apr 1865;
H. Schwarz, *Gesammelte Mathematische Abhandlungen* **1**, Springer, Berlin (1890).
- [29] D. Vanderbilt and J. Tersoff, *Phys. Rev. Lett.* **68**, 511 (1992).
- [30] T. Lenosky, X. Gonze, M. Teter, and V. Elser, *Nature* **355**, 333 (1992).
- [31] V. H. Crespi, *Phys. Rev. B* **58**, 12671 (1998).
- [32] M.-Z. Huang, W. Y. Ching and T. Lenosky, *Phys. Rev. B* **47**, 1593 (1993).
- [33] H. Aoki, M. Koshino, D. Takeda, H. Morise and K. Kuroki, *Phys. Rev. B* **65**, 035102 (2001).
- [34] F. Valencia, A. H. Romero, E. Hernández, M. Terrones and H. Terrones, *New J. Phys.* **5**, 123 (2003).
- [35] J. L. Peng, X. D. Fan and L. A. Bursill, *Int. J. Mod. Phys. B* **10**, 3875 (1996).

- [36] V. H. Crespi, L. X. Benedict, M. L. Cohen and S. G. Louie, Phys. Rev. B **53**, R13303 (1996).
- [37] N. Park, M. Yoon, S. Berber, J. Ihm, E. Osawa and D. Tomanek, Phys. Rev. Lett. **91**, 237204 (2003).
- [38] A. J. Stone and D. J. Wales, Chem. Phys. Lett. **128**, 501 (1986).
- [39] Kazutaka et al., Japan. J. Appl. Phys. **36**, L1479 (1997).
- [40] J. Kohanoff, J. Low Temp. Phys. **122**, 297 (2001).
- [41] J. S. Arellano, L. M. Molina, A. Rubio, and J. A. Alonso, J. Chem. Phys. **112**, 8114 (2000).
- [42] S. Hynek, W. Fuller and J. Bentley, Int. J. Hydrogen Energy **22**, 601 (1997).
- [43] F. Rodriguez-Reinoso and A. Linares-Solano in *Chemistry and Physics of Carbon* **22** (edited by P. A. Thrower) page 1, M. Dekker, Inc. (1989).
- [44] R. K. Agarwal, J. S. Noh, J. A. Schwarz and P. Davini, Carbon **25**, 219 (1987).
- [45] A. C. Dillon, K. M. Jones, T.A. Bekkedahl, C. H. Kiang, D. S. Bethune and M. J. Heben, Nature **386**, 377 (1997).
- [46] M. J. Heben, A. C. Dillon, T. Gennett, J. L. Alleman, P. A. Parilla, K. M. Jones and G. L. Hornyak, MRS Fall Meeting, Session A9.1, 17 (2000).
- [47] C. Liu, Y. Y. Fan, M. Liu, H. T. Cong, H. M. Cheng, and M. S. Dresselhaus, Science **286**, 1127 (1999).
- [48] P. Chen, X. Wu, J. Lin and K. L. Tan, Science, 285, 91 (1999).
- [49] C. Nutzenadel, H. Zuttel, D. Chartouni and L. Schlaphach, Electrochem Solid State Lett. **2**, 30 (1999);
N. Rajalakshmi, K. S. Dhathathreyan, A. Govindaraj and B. C. Satishkumar, Electrochimica Acta **45**, 4511 (2000);
S. M. Lee, K. S. Park, Y. C. Choi, Y. S. Park, J. M. Bok, D. J. Bae, K. S. Nahm, Y. G. Choi, S. C. Yu, N-g. Kim, T. Frauenheim and Y.H. Lee, Synth. Met. **113**, 209 (2000).
- [50] A. Chambers, C. Park, R. T. K. Baker and N. M. Rodriguez, J. Phys. Chem. B **102**, 4253 (1998).
- [51] Y. Ye, C. C. Ahn, C. Witham, B. Fultz, J. Liu, A. G. Rinzler, D. Colbert, K. A. Smith and R. E. Smalley Appl. Phys. Lett. **74**, 2307 (1999).

- [52] R. T. Yang, Carbon, **38**, 623 (2000);
 F. E. Pinkerton, B. G. Wicke, C. H. Olk, G. G. Tibbetts, G. P. Meisner, M. S. Meyer and J. F. Herbst, J. Phys. Chem. **104**, 9460 (2000);
 C. C. Ahn, Y. Ye, B. V. Ratnakumar, C. Witham, R. C. Bowman, Jr and B. Fultz, App. Phys. Lett. **73**, 3378 (1998);
 B. K. Gupta, O. N. Srivastava, Int. J. Hydrogen Engergy **25**, 825 (2000).
- [53] A. C. Dillon and M. J. Heben, Appl. Phys. A **72**, 133 (2001).
- [54] B. K. Pradhan, A. R. Harutyunyan, D. Stojkovic, J. C. Grossman, P. Zhang, M. Cole, V. Crespi, H. Goto, J. Fujiwara and P.C. Eklund, J. Mater. Research **17**, 2209 (2002).
- [55] D. Stojkovic, P. Zhang, P. E. Lammert and V. H. Crespi, Phys. Rev. B **68**, 195406 (2003).
- [56] D. Stojkovic, P. Zhang, V. H. Crespi, Phys. Rev. Lett. **87**, 125502 (2001).
- [57] D. Stojkovic, P. E. Lammert and V. H. Crespi, Phys. Rev. Lett., to be published.
- [58] D. Frankel and B. Smit, *Understanding Molecular Simulation: From Algorithms to Applications*, Academic Press (1996).
- [59] A. D. McNaught and A. Wilkinson, *IUPAC Compendium of Chemical Terminology*, Blackwell Science (1997). also at <http://www.iupac.org/goldbook/R05385.pdf>
- [60] G. E. Froudakis, J. Phys.: Cond. Matt. **14**, R453 (2002).
- [61] L. Jelaica, V. Sidis, Chem. Phys. Lett. **300**, 157 (1999).
- [62] X. Sha and B. Jackson, Surf. Sci. **496**, 318 (2002).
- [63] J. Pillath and J. Winter, J. Nucl. Materials, **176-177**, 319 (1990).
- [64] A. C. Dillon, K. M. Jones, T. A. Bekkedahl, C. H. Kiang, D. S. Bethune, M. J. Heben, Nature **386**, 377 (1997),
- [65] C.W. Bauschlicher, Jr., Chem. Phys. Lett. **322**, 237 (2000);
 C. W. Bauschlicher, Jr., Nano Lett. **1**, 223 (2001).
- [66] O. Gülseren, T. Yildirim and S. Ciraci, Phys. Rev. B **66**, 121401 (2002);
- [67] G. E. Froudakis, Nano Lett. **1**, 179 (2001).

- [68] S. M. Lee, K. H. An, Y. H. Lee, G. Seifert and T. Frauenheim, J. Am. Chem. Soc. **123** 5059 (2001).
- [69] K. F. Kelly, I. W. Chiang, E. T. Mickelson, R. H. Hauge, J. L. Margrave, X. Wang, G. E. Scuseria, C. Radloff and N. J. Halas, Chem. Phys. Lett. **313** 445 (1999).
- [70] E. T. Mickelson, C. B. Huffman, A. G. Rinzler, R. E. Smalley, R. H. Hauge, J. L. Margrave, Chem. Phys. Lett. **298**, 188 (1998).
- [71] P. J. Boul, J. Liu, E. T. Mickelson, C. B. Huffman, L. M. Ericson, I. W. Chiang, K. A. Smith, D. T. Colbert, R. H. Hauge, J. L. Margrave, R. E. Smalley, Chem. Phys. Lett. **310**, 367 (1999).
- [72] T. Mallouk, B. L. Hawkins, M. P. Conrad, K. Zilm, G. E. Maciel, N. Bartlett, Phil. Trans. Roy. Soc. London, Ser. A **314**, 179 (1985)
- [73] T. Yildirim, O. Gülseren and S. Ciraci, Phys. Rev. B **64**, 075404 (2001).
- [74] G. Kresse and J. Hafner, Phys. Rev. B **47**, 558 (1993);
G. Kresse, J. Furthmüller, Comp. Mat. Sci. **6**, 15 (1996)
- [75] R. Rurali, E. Hernández, Comp. Mater. Sci. **28**, 85 (2003).
- [76] P. M. Ajayan, T. W. Ebbesen, T. Ichihashi, S. Iijima, K. Tanigaki, and H. Hiura, Nature London **362**, 522 (1993);
M. S. C. Mazzoni, H. Chacham, P. Ordejon, D. Sanchez-Portal, J. M. Soler, and E. Artacho, Phys. Rev. B **60** R2208 (1999).
- [77] E.-C. Lee, Y.-S. Kim, Y.-G. Jin, and K. J. Chang, Phys Rev. B, **66**, 073415 (2002)
- [78] S. Iijima, Nature **354**, 56 (1991).
- [79] A. Krishnan, E. Dujardin, M. M. J. Treacy, J. Hugdahl, S. Lynum, T. W. Ebbesen, Nature **388**, 451 (1997).
- [80] M. Damnjanovic, I. Milosevic, T. Vukovic, and R. Sredanovic, Phys. Rev. B **60**, 2728 (1999).
- [81] G. A. Olah (editor), *Cage Hydrocarbons*, J.Wiley & Sons, Inc., New York (1990); E. Osawa and O. Yonemitsu (editors), *Carbocyclic Cage Compounds: Chemistry and Applications*, VCH Publishers, Inc., New York (1992).
- [82] N. Hamada, S. Sawada, and A. Oshiyama, Phys. Rev. Lett. **68**, 1579 (1992);
J. W. Mintmire, B.I. Dunlap and C.T. White, Phys. Rev. Lett. **68**, 631 (1992);
R. Saito, M. Fujita, G. Dresselhaus, M.S. Dresselhaus, Appl. Phys. Lett. **60**, 2204 (1992).

- [83] S. Sawada and N. Hamada, Solid State Commun. **83**, 917 (1992).
- [84] L.-M. Peng, Z. L. Zhang, Z. Q. Xue, Q. D. Wu, Z. N. Gu, and D. G. Pettifor, Phys. Rev. Lett. **85**, 3249 (2000).
- [85] H.Y. Peng, N Wang, Y.F. Zheng, and Y. Lifshitz, App. Phys. Lett. **77**, 2831 (2000).
- [86] N. Wang, Z.K. Tang, G.D. Li, J.S. Chen, Nature **408**, 50 (2000).
- [87] G. Seifert, Th. Köhler, H.M. Urbassek, E. Hernández and Th. Frauenheim, Phys. Rev. B **63**, 193409 (2001).
- [88] The LDA DFT calculations for CH systems give typically pretty accurate relative binding energy, but the absolute value tends to be off, which is why we present our results in terms of energy differences. To have an absolute scale, the experimental binding energy of benzene is 59.27 eV, according to W.C. Ermler and C.W. Kern, J. Chem. Phys. **58**, 3458 (1973). See also <http://archive.ncsa.uiuc.edu/Apps/CMP/hydroc.html>
- [89] K. Nakada, M. Fujita, G. Dresselhaus, M. S. Dresselhaus, Phys. Rev. B **54**, 17954 (1996).
- [90] J.P. Lu, Phys. Rev. Lett. **79**, 1297 (1997).
- [91] A. Krishnan, E. Dujardin, T.W. Ebbesen, P.N. Yianilos and M.M.J. Treacy, Phys. Rev. B **58**, 14013 (1998).
- [92] R. H. Baughman, A. A. Zakhidov, W. A. de Heer, Science **297**, 787 (2002).
- [93] D. J. Browning, M. L. Gerrard, J. B. Lakeman, I. M. Mellor, R. J. Mortimer and M. C. Turpin, Nano Lett. **2**, 201 (2002).
- [94] O. Gülseren, T. Yildirim and S. Ciraci, Phys. Rev. Lett. **87**, 116802 (2001).
- [95] W. Helfrich, Z. Naturforsch. **28c**, 693 (1973).
- [96] M. Fujita, K. Wakabayashi, K Nakada, and K. Kusakabe, J. Phys. Soc. Jap. **65**, 1920 (1996).
- [97] Y. Li , S. Xie, W. Zhou, D. Tang, X. Zou, Z. Liu, G. Wang Carbon **39**, 615 (2001).
- [98] M. Maruyama and K. Kusakabe, J. Phys. Soc. Jpn. **73**, 656 (2004).
- [99] M. Maruyama and K. Kusakabe, Phys. Rev. B **67**, 092406 (2003).
- [100] M. Rohlfing and S. G. Louie, Phys. Rev. B **62**, 4927 (2000).

- [101] C. D. Spataru, S. Ismail-Beigi, L. X. Benedict and S. G. Louie, Phys Rev. Lett. **92**, 077402 (2004).
- [102] G. M. Odegard, T. S. Gates, L. M. Nicholson and K. E. Wise, Compos. Sci. Tech. **62**, 1869 (2002).
- [103] D. H. Robertson, D. W. Brenner, and J. W. Mintmire, Phys. Rev. B **45**, 12592 (1992).
- [104] J. O’Keeffe, C. Wei, and K. Cho, App. Phys. Lett. **80**, 676 (2002).
- [105] K. H. Khoo, M. S. C. Mazzoni, and S. G. Louie, Phys. Rev. B **69**, 201401(R) (2004).
- [106] A. E. Albanesi, C. M. I. Okoye, C. O. Rodriguez, E. L. Peltzer y Blanca and A. G. Petukhov, Phys. Rev. B **61**, 16589 (2000).
- [107] C. M. Okoye, J. Phys.: Cond. Matter **14**, 8625 (2002).
- [108] We use the parametrization of D. Porezag, Th. Frauenheim, Th. Köhler, G. Seifert, and R. Kaschner, Phys. Rev. B **51**, 12947 (1995); J. Widany, Th. Frauenheim, Th. Köhler, M. Sternberg, D. Porezag, G. Jungnickel, and G. Seifert, Phys. Rev. B **53**, 4443 (1996).

Vita

Dragan Stojkovic

Education

- 2004 PhD Physics Major and High Performance Computing Graduate Minor, Pennsylvania State University
- 1998 Masters of Science, Physics, University of Belgrade, Belgrade, Yugoslavia
- 1993 Bachelor of Science, Physics, University of Belgrade, Belgrade, Yugoslavia

Awards

- 2003 David C Duncan Graduate Fellowship, Physics Department, Pennsylvania State University
- 1998 The Best Master Thesis Award, Faculty of Physics, University of Belgrade, Yugoslavia
- 1994 The Best Bachelor Thesis Award, Faculty of Physics, University of Belgrade, Yugoslavia
- 1994 Valedictorian, Faculty of Physics, University of Belgrade, Yugoslavia

Publications

- D. Stojkovic, P. E. Lammert and V. H. Crespi, "Electronic Bisection of a Single Wall Carbon Nanotube by Controlled Chemisorption", to be published in Physical Review Letters.
- D. Stojkovic, P. Zhang, P. E. Lammert and V. H. Crespi, "Collective stabilization of hydrogen chemisorption on graphenic surfaces", Physical Review B 68, 195406 (2003).
- J. Lazovic-Stojkovic, Q. X. Yang, D. Stojkovic, W. Z. Liu, J. T. Vaughan, M. B. Smith, "Hexagonal coil: A single channel multi-coil design for small animal imaging", Developmental Neuroscience 24, 452 (2002). An article has been accepted in Magnetic Resonance in Medicine.
- B. K. Pradhan, A. R. Harutyunyan, D. Stojkovic, J. C. Grossman, P. Zhang, M. Cole, V. Crespi, H. Goto, J. Fujiwara and P.C. Eklund, "Large cryogenic storage of hydrogen in carbon nanotubes at low pressures", Journal of Materials Research 17, 2209 (2002).
- D. Stojkovic, P. Zhang and V. H. Crespi, "The smallest nanotube: breaking the symmetry of sp^3 bonds in tubular geometries", Physical Review Letters 87, 125502 (2001).
- M. Damnjanovic, I. Milosevic and D. Stojkovic, "Casimir operators and group projectors", Journal of Physics A 29, 7983 (1996).